Fluid–Electromagnetic Modelling of Atmospheric Pressure CO_2 Microwave Plasma: Towards Reactor Design

Vojtěch Laitl[1,2,‡,*], Ivan Tsonev[1,2,‡], Omar Biondo[1,2], Emile Carbone[3], Matthias C. K. Albrechts[1,2], and Annemie Bogaerts[1,2]

[1]Research Group PLASMANT and Centre of Excellence PLASMA, University of Antwerp, Groenenborgerlaan 171, BE2020 Antwerp, Belgium
[2]Electrification Institute, University of Antwerp, Olieweg 97, BE2020 Antwerpen, Belgium
[3]Institut National de la Recherche Scientifique, Université du Québec, Varennes, QC J3X 1P7, Canada
[‡]Shared first authors.
[*]Corresponding author. E-mail address: vojtech.laitl@student.uantwerpen.be (Vojtěch Laitl)

Supporting Information (SI)

S1 Flow Field Simulations

This work features both 3–D (ambient CO_2) and 2–D axisymmetric (fully coupled model) fluid flow calculations. The former uses the standard Cartesian position vector $\mathbf{r} = [x; y; z]^\intercal$ and the corresponding Reynolds-averaged velocity field of $\bar{\mathbf{u}} = [\bar{u}_x; \bar{u}_y; \bar{u}_z]^\intercal$. The latter expresses velocity in cylindrical coordinates, *i.e.*, referring to the radial (r), circumferential (φ), and axial (z) direction. The conversion of one framework to another is provided by

$$\begin{cases} r^2 = x^2 + y^2 & \bar{u}_r = \frac{\partial r}{\partial x}\frac{\partial x}{\partial t} + \frac{\partial r}{\partial y}\frac{\partial y}{\partial t} = \frac{x\bar{u}_x + y\bar{u}_y}{\sqrt{x^2+y^2}} \\ \tan(\varphi) = \frac{y}{x} & \bar{u}_\varphi = r\left(\frac{\partial \varphi}{\partial x}\frac{\partial x}{\partial t} + \frac{\partial \varphi}{\partial y}\frac{\partial y}{\partial t}\right) = \frac{\sqrt{x^2+y^2}}{1+\left(\frac{y}{x}\right)^2} \cdot \frac{-y\bar{u}_x + x\bar{u}_y}{x^2} \; . \\ z = z & \bar{u}_z = \bar{u}_z \end{cases} \tag{S1}$$

Both the 3–D and 2–D axisymmetric RANS simulations employ the Menter shear stress transport (SST) model. The model is described below, with governing equations assuming 3–D geometry. The formulation of SST equations in cylindrical coordinates is done in analogy to Eq. (S1) and is automated in COMSOL.

S1.1 Menter Shear Stress Transport Model

SST conveniently combines the robustness of k–ε with the more precise performance of k–ω models [1]. Consequently, it has often been chosen for various industrial applications, including plasma reactor engineering (*e.g.*, [2, 3]).

Within SST, the auxiliary turbulence variables k and ω are governed by the following equations,

$$\bar{\rho}(\bar{\mathbf{u}} \cdot \nabla)k = \nabla \cdot ((\mu + \mu_\mathsf{T}\sigma_k)\nabla k) + P_\mathrm{lim} + \beta_0^\star \bar{\rho}\omega k \tag{S2}$$

and

$$\bar{\rho}(\bar{\mathbf{u}} \cdot \nabla)\omega = \nabla \cdot ((\mu + \mu_\mathsf{T}\sigma_\omega)\nabla \omega) + \frac{\gamma}{\mu_\mathsf{T}}\bar{\rho}P_\mathrm{lim} - \beta_0^\star \bar{\rho}\omega^2 + 2(1 - f_{v1})\left(\frac{\sigma_{\omega 2}\bar{\rho}}{\omega}\right)\nabla k \cdot \nabla \omega, \tag{S3}$$

as repeated from the main text. σ_k, σ_ω, and γ are scaling constants defined by formulae

$$\sigma_k = f_{v1}\sigma_{k1} + (1 - \sigma_{v1})\sigma_{k2}, \tag{S4}$$

$$\sigma_\omega = f_{v1}\sigma_{\omega 1} + (1 - f_{v1})\sigma_{\omega 2}, \tag{S5}$$

and

$$\gamma = f_{v1}\gamma_1 + (1 - f_{v1})\gamma_2 \tag{S6}$$

whose right-hand side parameters are listed in Tab. S1 below.

Table S1: Dimensionless scaling constants of the SST model.

Constant	Canonical value	Constant	Canonical value
σ_{k1}	0.85	σ_{k2}	1
$\sigma_{\omega 1}$	0.5	$\sigma_{\omega 2}$	0.856
γ_1	0.5556	γ_2	0.44

$\beta_0^\star = 0.09$ in Eq. (S2)–(S3) is a dimensionless model constant. Its value is also used to define the inlet specific turbulent dissipation rate ω_0 in Tab. 2, main text.

f_{v1} is a blending function of the form

$$f_{v1} = \tanh\left(\min\left\{\theta_2^2, \frac{4\sigma_{\omega 2}k}{\mathrm{CD}_{k\omega}y^2}\right\}\right) \tag{S7}$$

which is responsible for interpolating between k–ε (for which $f_{v1} = 1$ in the free stream) and k–ω transport equations. The $\mathrm{CD}_{k\omega}$ and θ_2 placeholders are defined as

$$\mathrm{CD}_{k\omega} = \max\left\{2\bar{\rho}\sigma_{\omega 2}\cdot\frac{1}{\omega}\cdot\left(\frac{\partial k}{\partial x}\right)\left(\frac{\partial \omega}{\partial x}\right), 10^{-10}\right\} \tag{S8}$$

and

$$\theta_2 = \max\left\{\frac{2\sqrt{k}}{\beta_0^\star \omega \ell_w^2}, \frac{500\mu}{y^2\omega}\right\} \tag{S9}$$

in which ℓ_w is the wall distance. Finally, P_{lim} in Eq. (S4)–(S5) is a product-limiting coefficient:

$$P_{\mathrm{lim}} = \min\left\{P_k, 10\bar{\rho}\beta_0^\star k\omega\right\} \tag{S10}$$

in which

$$P_k = \mu_{\mathsf{T}}\left(\nabla\bar{\mathbf{u}} : (\nabla\bar{\mathbf{u}} + (\nabla\bar{\mathbf{u}})^{\mathsf{T}}) - \frac{2}{3}(\nabla\cdot\bar{\mathbf{u}})^2\right) - \frac{2}{3}\bar{\rho}k\nabla\cdot\mathbf{u} \tag{S11}$$

(: is the Frobenius product). The above equations are used to formulate the turbulent viscosity μ_{T} as

$$\nu_{\mathsf{T}} = \frac{\bar{\rho}a_1 k}{\max\{a_1\omega, \mathbf{S}f_{v2}\}}. \tag{S12}$$

$\mathbf{S}$ is the magnitude of the absolute shear rate, *i.e.*,

$$\mathbf{S} = \sqrt{2\mathbb{S} : \mathbb{S}} \tag{S13}$$

in which

$$\mathbb{S} = \nabla\mathbf{u} + (\nabla\mathbf{u})^{\mathsf{T}}. \tag{S14}$$

$a = 0.31$ is a dimensionless constant. Finally,

$$f_{v2} = \tanh(\theta_2^2) \tag{S15}$$

is another hyperbolic tangent blending function. μ_{T} is then used to calcuate the friction tensor $\mathbb{K}$,

$$\mathbb{K} = (\mu + \mu_{\mathsf{T}})(\nabla\bar{\mathbf{u}} + (\nabla\bar{\mathbf{u}})^{\mathsf{T}}) - \frac{2}{3}(\mu + \mu_{\mathsf{T}})(\nabla\cdot\bar{\mathbf{u}})\mathbb{I} - \frac{2}{3}\bar{\rho}k\mathbb{I}, \tag{S16}$$

which appears in Eq. (2), main text.

S1.2 3–D Ambient Flow Simulations

The modelling work begins with 3–D flow field simulations of ambient CO_2 ($T = 293.15$ K; $p = 930$ mbar) in a reactor geometry that copies Fig. 1(left), main text. The discussion below is limited to the results of the SST model since, as mentioned in the main text, the complementary laminar flow solution yields comparable (±0.1) swirl numbers.
The flow geometry is replotted in Fig. S1 below, along with a colour identification of boundary conditions introduced in Tab. S2. For simplicity, only 2 tangential inlets are marked in the figure; the remaining inlets are placed symmetrically around the perimeter.

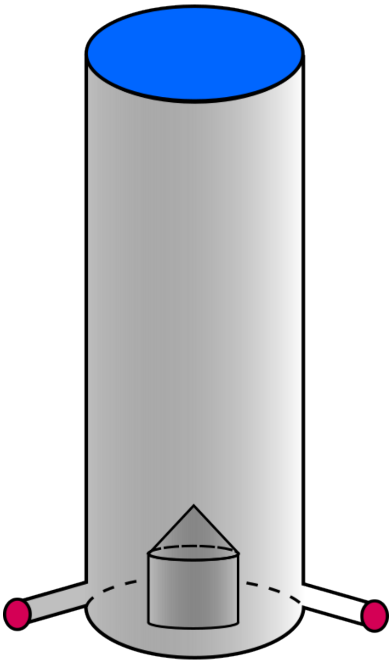

Figure S1: Sketch of the experimental geometry (excerpt from Fig. 1). The colouring identifies the placement of the boundary conditions introduced below.

A fully developed velocity field is set at the red inlets, which mimics the inflow from (sufficiently long) upstream pipelines. At the blue outflow, we apply a pressure constraint, and all remaining boundaries are treated as no-slip walls. The boundary conditions are summarised in Tab. S2.

Table S2: List of boundary conditions involved in the 3–D simulations.

Boundary	Colour label	Boundary equation
inflow**	red	$\bar{u} = \frac{\phi}{4\pi r_{\text{in}}^2} \cdot \left(\frac{p_\circ}{930\ \text{mbar}}\right); \quad \bar{\mathbf{u}} \cdot \mathbf{t} = 0$
outflow	blue	$p - 930\ \text{mbar} = 0$
wall	black	$\bar{\mathbf{u}} = \mathbf{0}$

** applied to all four disjoint surfaces separately

$\mathbf{t}$ in Tab. S2 is a unit vector in tangential direction, $r_{\text{in}} = 2.15$ mm is the inner radius of the tangential inlets, and ϕ is the standard flow rate in SLM. Its conversion onto a volumetric flow rate is done at $T = T_\circ$ and $p_\circ = 1$ atm. This ensures that the mass flow rate through the reactor equals

$$\dot{m} = \frac{\phi}{1\ \text{SLM}} \cdot \frac{0.001\ \text{m}^3\ \text{L}^{-1}}{60\ \text{s min}^{-1}} \cdot \frac{p_\circ M}{R T_\circ}, \tag{S17}$$

as is the case for the experimental mass flow controller calibrated at $T_\circ$ and $p_\circ$ [4].
$M = 44.01 \times 10^{-3}$ kg mol^{-1} is the molar mass of CO_2.

S1.2.1 Mesh Independence Study

The mass flow rate in Eq. (S17) is used as a metric for a mesh independence study. In particular, we verify the mesh convergence by defining a testing mass flow rate,

$$\dot{m}_{\text{test}} = \int\limits_{\text{inflow}} \bar{\rho}\bar{\mathbf{u}} \cdot \mathrm{d}\mathbf{S} = \int\limits_{\text{outflow}} \bar{\rho}\bar{\mathbf{u}} \cdot \mathrm{d}\mathbf{S}, \tag{S18}$$

across both the inflow and outflow boundary ($\mathrm{d}\mathbf{S} = \mathbf{n}\mathrm{d}S$ is a surface increment in their normal direction). In each simulation, we check that the left- and right-hand side of Eq. (S18) are equal to each other and record the difference between $\dot{m}_{\text{test}}$ and $\dot{m}$ on a gradually refined mesh. The meshes are created by downsizing the default COMSOL options for 3–D fluid dynamics with tetrahedral element shapes [5].

The results of the test are indicated in Tab. S3. Besides the recorded mass flow rates, we make note of the computational time required at the i9-13900k CPU (128 GB of DDR4 RAM). The last row for each ϕ corresponds to its mass flow rate $\dot{m}$ in Eq. (S17), *i.e.*, to the theoretical value obtained in a continuous domain at infinite time.

All further data in this section are obtained with the finest tests in Tab. S3. For consistency, its size partitioning is adopted in the 2–D axisymmetric models as well. This corresponds to the size of 0.0075–0.65 mm for a domain element and 0.001–0.335 mm for a boundary element. Creating the 2–D mesh using triangular elements then gives the final number of 137,626 domain elements and 4,014 boundary elements mentioned in Sec. 2.4, main text.

Table S3: Results of the mesh refining study involving the 3–D ambient flow simulations.

Domain elements (mm)	Boundary elements	Edge elements	$\dot{m}_{\mathrm{inflow}}$ (kg s^{-1})	$\dot{m}_{\mathrm{outflow}}$ (kg s^{-1})	relative error	CPU time
			$\phi = 10$ SLM			
1,210,342	62,756	368	2.9716×10^{-4}	2.9716×10^{-4}	2.5%	5 hours
3,573,259	132,796	526	3.0083×10^{-4}	3.0083×10^{-4}	1.3%	24 hours
11,308,353	325,518	850	3.0322×10^{-4}	3.0322×10^{-4}	0.6%	168 hours
∞	∞	∞	3.0423×10^{-4}	3.0423×10^{-4}	0	∞
			$\phi = 20$ SLM			
1,210,342	62,756	368	5.9449×10^{-4}	5.9449×10^{-4}	2.5%	5 hours
3,573,259	132,796	526	6.0183×10^{-4}	6.0183×10^{-4}	1.3%	24 hours
11,308,353	325,518	850	6.0662×10^{-4}	6.0662×10^{-4}	0.6%	168 hours
∞	∞	∞	6.0985×10^{-4}	6.0985×10^{-4}	0	∞
			$\phi = 40$ SLM			
1,210,342	62,756	368	1.1886×10^{-3}	1.1886×10^{-3}	2.5%	10 hours
3,573,259	132,796	526	1.2033×10^{-3}	1.2033×10^{-3}	1.3%	48 hours
11,308,353	325,518	850	1.2129×10^{-3}	1.2129×10^{-3}	0.6%	336 hours
∞	∞	∞	1.2169×10^{-3}	1.2169×10^{-3}	0	∞

S1.2.2 Example Results

The refined 3–D simulations result in a well-converged velocity field which resolves the vortex structure of swirl flows. For illustration, Fig. S2 plots the $\bar{u}_z$ velocity (a) and the turbulent kinetic energy (b) of a 20 SLM flow field in an $x = 0$ cut plane of the 3–D geometry.

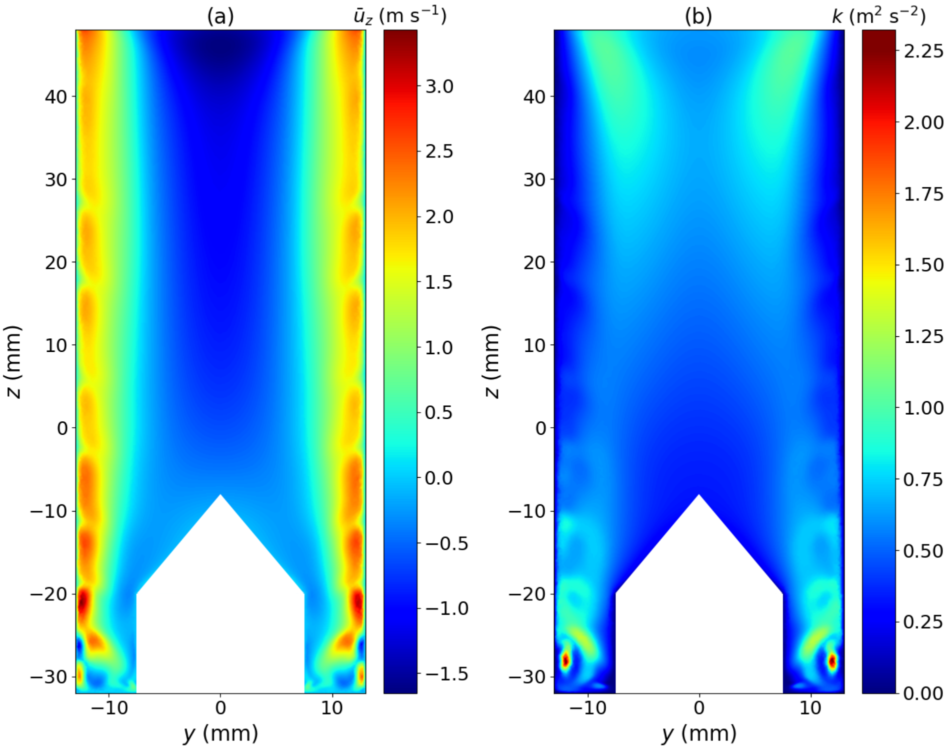

Figure S2: $\bar{u}_z$ (a) and k (b) calculated for ambient CO_2 at 20 SLM. The plot is drawn in an $x = 0$ section of the 3–D geometry.

The plot shows a centrifugal gradient in $\bar{u}_z$, along with negative axial velocities reached in the top centre part of the domain. This pattern is a typical feature of precessing vortices sustained at ambient conditions [6]. The centrifugal gradient also generates the highest turbulence in the system, which is demonstrated by the turbulent kinetic energies of $k > 2$ m^2 s^{-2} at the bottom of the domain.

For 10 and 40 SLM, the flow pattern is qualitatively the same, whereas the magnitude of both $\bar{\mathbf{u}}$ and k is, as expected, lower in the 10 SLM case and higher in the 40 SLM case, respectively.

S1.2.3 Flow Field Averaging

Finally, the 3–D flow field is averaged using its swirl numbers and turbulent intensities, which are used as an input to the 2–D axisymmetric model in the main text. The averaging is done 20 mm below the cylindrical resonator, where our 3–D results first show approximate axisymmetry. An example of this symmetry is given in Fig. S3.

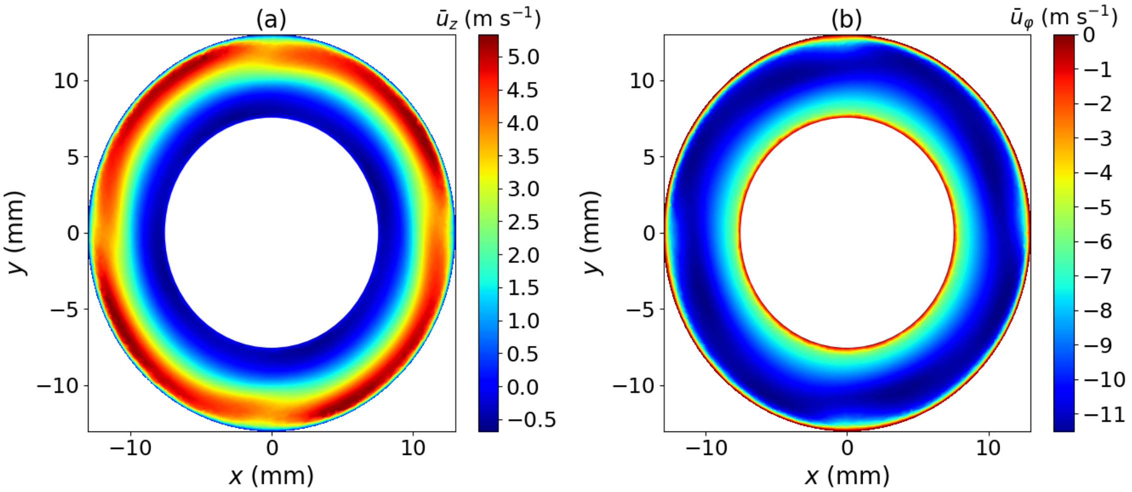

Figure S3: An example of axial (a) and circumferential (b) velocity solved by the 3–D model at $\phi = 40$ SLM. The data are plotted in an x–y plane 20 mm below the cylindrical resonator. See Eq. (S1) for the definition of the velocity components.

The velocities shown in Fig. S3 are used to calculate the corresponding swirl numbers as

$$\mathcal{S}_0 := \frac{\dot{I}_\varphi}{R\dot{I}_z} = \frac{\int\limits_{r=7.5\,\mathrm{mm}}^{R} r\bar{\rho}\bar{u}_\varphi\bar{u}_z\,\mathrm{d}(\pi r^2)}{R\int\limits_{r=7.5\,\mathrm{mm}}^{R} \bar{\rho}\bar{u}_z^2\,\mathrm{d}(\pi r^2)}\,[6], \tag{S19}$$

in which $\dot{I}$ is a momentum flux, $r = \sqrt{x^2 + y^2}$, $R = 13$ mm, and πr^2 is a surface area at given r. Solving Eq. (S19) for all flow rates gives the data in Tab. 3, main text.
The turbulent intensities are calculated likewise. Fig. S4 shows an example of velocity magnitude and turbulent kinetic energy which are used in the following definition of turbulent intensity

$$I_\mathsf{T} := \frac{\sqrt{\frac{2}{3}k}}{\bar{u}}[7]. \tag{S20}$$

To get the $I_{\mathsf{T}0}$ data in Tab. 3, Eq. (S20) is averaged over the annulus Ω (as coloured in Fig. S4), which gives

$$I_{\mathsf{T}0} = \frac{\iint\limits_{\Omega} I_\mathsf{T}\,\mathrm{d}\Omega}{\iint\limits_{\Omega} \mathrm{d}\Omega}. \tag{S21}$$

Tab. 3 contains the solutions of Eq. (S21) for all flow rates, which completes the specifications of the inlet boundary. The 2–D axisymmetric inlet is then centered 20 mm below the cylindrical resonator, which corresponds to the position of our averaging cut planes.

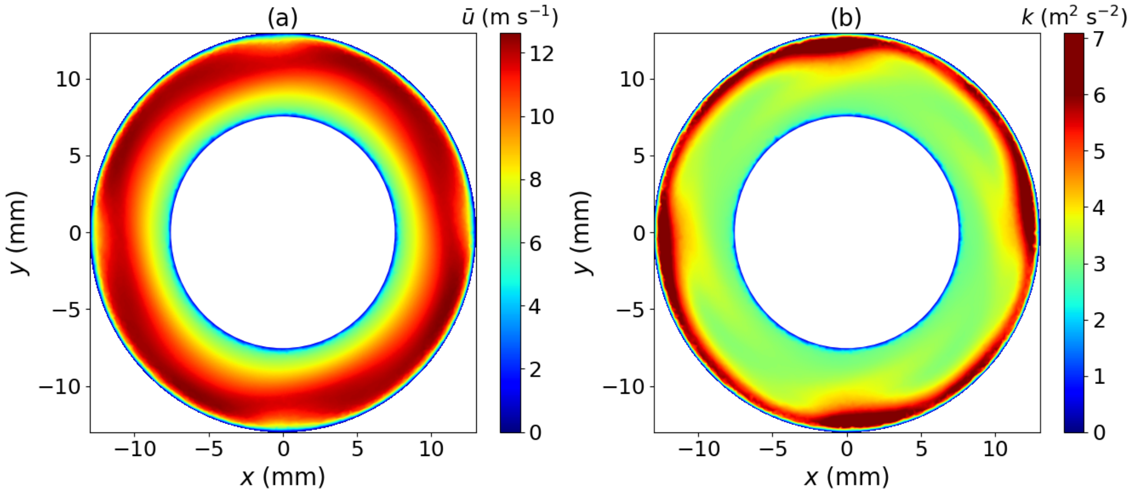

Figure S4: An example of velocity magnitude (a) and turbulent kinetic energy (b) solved by the 3–D model at $\phi = 40$ SLM. The data are plotted in an x–y plane 20 mm below the cylindrical resonator.

S2 Reactive Flow Simulations

The transport coefficients of the reactive gas, *i.e.*, its heat capacity, thermal conductivity, dynamic viscosity, and diffusivity, are defined by mixture averaging, as introduced in the main text. NASA9 polynomials [8] are used to define the heat capacities of pure species, and the Chapman–Enskog theory is used for the remaining molecular properties.

S2.1 Chapman–Enskog Transport Coefficients

The binary diffusion coefficients D_{ik} (Eq. (8), main text) are defined as

$$D_{ik} = 2.6628 \times 10^{-22} \cdot \frac{\sqrt{\frac{T^3(M_i+M_k)}{2\times 10^3 M_i M_k}}}{p\sigma_{\mathrm{LJ},i}\sigma_{\mathrm{LJ},k}} \cdot \Omega_D^{-1} \tag{S22}$$

where T and p are the absolute temperature and pressure, $M_{i,k}$ are molar masses, and $\sigma_{\mathrm{LJ},i,k}$ are characteristic lengths of a molecular potential. In our case, Lennard-Jones potentials are used, with the characteristic parameters obtained from [8] (CO_2, CO, O_2, C, O) and [9] (C_2). Finally, Ω_D denotes the collision integral, calculated according to [10] as

$$\Omega_D = \frac{c_1}{\bar{T}_{\mathrm{red}}^{c_2}} + \frac{c_3}{\exp(c_4\bar{T}_{\mathrm{red}})} + \frac{c_5}{\exp(c_6\bar{T}_{\mathrm{red}})} + \frac{c_7}{\exp(c_8\bar{T}_{\mathrm{red}})}. \tag{S23}$$

c_1–c_8 are empirical constants, and

$$\bar{T}_{\mathrm{red}} = \sqrt{T_{\mathrm{red},i}T_{\mathrm{red},k}} = \frac{k_{\mathrm{B}}T}{\sqrt{\epsilon_{\mathrm{LJ},i}\epsilon_{\mathrm{LJ},k}}} \tag{S24}$$

is the geometric mean reduced temperature, obtained with the Lennard-Jones well depths $\epsilon_{\mathrm{LJ},i,k}$. A truncated form of Ω_D, the collisional integral Ω_λ,

$$\Omega_\lambda = \frac{b_1}{T_{\mathrm{red}}^{b_2}} + \frac{b_3}{\exp(b_4T_{\mathrm{red}})} + \frac{b_5}{\exp(b_6T_{\mathrm{red}})}, \tag{S25}$$

is used to define the thermal conductivity of a species. This property is equal to

$$\lambda_i = 2.669 \times 10^{-6} \cdot \frac{\sqrt{TM_i \cdot 10^3}}{\sigma_{\mathrm{LJ},i}^2\Omega_\lambda} \cdot \frac{1.15C_{p,i} + 0.88R}{M_i} \tag{S26}$$

in which $C_{p,i}$ is the heat capacity of i interpolated from [8]. λ_i are used in Eq. (15), main text. Finally, the dynamic viscosity μ is expressed as

$$\begin{aligned}
\mu &= \sum_{i=\mathrm{species}} \frac{\mu_i}{1 + \frac{1}{x_i}\sum\limits_{k\neq i} x_k\phi_{ik}};\\
\phi_{ik} &= \frac{1}{\frac{4}{\sqrt{2}} \cdot \left(1 + \frac{M_i}{M_k}\right)^{\frac{1}{2}}};\\
\mu_i &= 2.669 \times 10^{-6} \cdot \frac{\sqrt{TM_i \cdot 10^3}}{\sigma_{\mathrm{LJ},i}^2\Omega_\mu};\\
\Omega_\mu &= \frac{b_1}{T_{\mathrm{red}}^{b_2}} + \frac{b_3}{\exp(b_4T_{\mathrm{red}})} + \frac{b_5}{\exp(b_6T_{\mathrm{red}})}.
\end{aligned} \tag{S27}$$

μ defines the friction tensor $\mathbb{K}$ used in Eq. (2), main text.

S3 Global Electrical Properties

According to [11], microwave discharges should always be treated as two-temperature systems. Namely, a distinction should be made between gas temperature and electron temperature, and the electrical properties should be treated as a function of both. This, however, requires multifluid modelling of extensive chemistries, which is beyond the capability of current computational resources [12]. To maintain consistency with our computationally light, single-fluid model (Sec. 2, main text), we therefore provide this description implicitly and calculate the electrical properties by means of a global (0–D) model.

S3.1 0–D Model Description

A global model can be understood as a transport-free simplification of Eq. (5), main text. Ignoring the effects of convection and diffusion makes the model easy to solve, which allows to incorporate extensive chemistry sets. We specifically leverage this advantage to describe charge particle kinetics in the system.
The governing equations of the model are of the form

$$\rho \frac{\mathrm{d}w_i}{\mathrm{d}t} = M_i R_i \tag{S28}$$

and

$$e \frac{\mathrm{d}\langle\epsilon\rangle}{\mathrm{d}t} = R_\epsilon + e\dot{q}_{\mathrm{rh}}. \tag{S29}$$

R_i is the total volumetric reaction rate of i-th species and $\langle\epsilon\rangle$ in is the electron energy density whose source terms involve the electron energy exchange rate R_ϵ and the microwave power density $\dot{q}_{\mathrm{rh}}$.
R_i is defined in analogy to Eq. (9), main text, and involves all reactions in the kinetic scheme. R_ϵ is specific to electron reactions and is expressed as follows:

$$R_\epsilon = \sum_{j=\text{electron reactions}} r_j \Delta\epsilon_j. \tag{S30}$$

r_j are the rates of the electron reactions and $\Delta\epsilon_j$ is the change of electron energy that accompanies them.
Solving the governing equations (S28)–(S29) requires both the gas temperature T and electron temperature T_e. T is an input parameter to the model and is varied in the range of $T \in [1000\ \mathrm{K}; 8000\ \mathrm{K}]$. T_e is calculated within the model as

$$T_e = \frac{2}{3}\frac{\langle\epsilon\rangle}{N_e}. \tag{S31}$$

$\langle\epsilon\rangle$ is solved by Eq. (S29) and the electron number density N_e results from Eq. (S28) for $i =$ electron. To close the model, we treat $\dot{q}_{\mathrm{rh}}$ as another input parameter and vary its values in the range of $\dot{q}_{\mathrm{rh}} \in [10^5\ \mathrm{W\ m^{-3}}; 10^{10}\ \mathrm{W\ m^{-3}}]$.
The global chemistry set involves 23 species given in Tab. S4(top). This list is extended over the main text by including the two lowest electronic excitations and single-charged positive ions corresponding to all neutral species. Only for C_2, the electronic excitation is neglected, as its total mole fraction is expected to be $< 10^{-5}$ [4]. Any negative ions are neglected as well, since at the operating pressure, their contribution to the chemical kinetics is marginal [13, 14]. Quasi-neutrality is therefore assumed between positive ions and electrons.
In addition to the above, electron-impact vibrational excitations of CO_2, CO, and O_2 electronic ground states are included in the model, as described by vibrational quantum number configurations in Tab. S4(bottom). For CO and O_2, we enumerate the vibrational quantum number

υ; for CO_2, the notation describes its three vibrational quantum numbers of (υ_{sym} δ υ_{anti}) [15]. υ_{sym} is the symmetric stretching mode, δ is the (double degenerate) bending mode, and υ_{anti} is the antisymmetric stretching mode. For completeness, also the fundamental wavenumbers are noted in the table.

Table S4: List of chemical species and electronic states (top) and their vibrational states (bottom) included in the global model.

Neutral species	CO_2, CO, C, O, O_2, C_2
Electronic states	$CO_2(A)$, $CO_2(B)$, $CO(a^3\Pi)$, $CO(a'^3\Sigma^+)$, $C(^1D)$ $C(^1S)$, $O(^1D)$, $O(^1S)$, $O_2(^1\Delta_g)$, $O_2(^1\Sigma_g^+)$
Charged particles	${CO_2}^+$, CO^+, C^+, O^+, ${O_2}^+$, ${C_2}^+$, e^-

CO_2 vibrational excitations ($\tilde{\nu}_{\mathrm{sym}} = 1335.88$ cm^{-1}; $\tilde{\nu}_\delta = 667.20$ cm^{-1}; $\tilde{\nu}_{\mathrm{anti}} = 2361.65$ cm^{-1})
$CO_2(100)$, $CO_2(200)$, $CO_2(300)$, $CO_2(010)$, $CO_2(020)$, $CO_2(030)$, $CO_2(040)$, $CO_2(050)$
$CO_2(001)$, $CO_2(002)$, $CO_2(003)$, $CO_2(004)$, $CO_2(005)$, $CO_2(110)$, $CO_2(120)$, $CO_2(130)$
$CO_2(011)$, $CO_2(021)$, $CO_2(101)$, $CO_2(210)$, $CO_2(060+220+140)$, $CO_2(0n0+n00,\ n = 3\text{–}21)$

CO vibrational excitations ($\tilde{\nu} = 2169.81$ cm^{-1})
$\upsilon = 1\text{–}10$

O_2 vibrational excitations ($\tilde{\nu} = 1580.19$ cm^{-1})
$\upsilon = 1\text{–}4$

The heavy particle kinetics copies Tab. 1, main text. Below, we describe the extensions to the kinetic scheme, *i.e.*, our treatment of electron kinetics, charged particle kinetics, and the kinetics of vibrational states, respectively.

S3.1.1 Electron Kinetics

For the specified range of temperatures (< 8000 K), the electron kinetics consists of electron-impact reactions with heavy particles (electron–electron collisions are neglected) [16]. Typically, for an impact reaction j,

$$j : \mathrm{M} + \mathrm{e}^- \longrightarrow \text{products},$$

r_j is of the form $r_j = k_j[\mathrm{M}]N_e$, where [M] is the concentration of the heavy particle and the rate coefficient k_j depends on EEDF. k_j is often calculated using the reaction cross section σ_j by the equation

$$k_j = \left(\frac{2}{m_e}\right)^{\frac{1}{2}} \int_{\epsilon_0}^{\infty} \epsilon \sigma_j(\epsilon) f_\epsilon(\epsilon) \mathrm{d}\epsilon, \tag{S32}$$

i.e., formally, as the mean value of the $\sigma_j v$ product with respect to electron velocity distribution. v is the electron drift velocity, expanded according to

$$v = \left(\frac{2\epsilon}{m_e}\right)^{\frac{1}{2}}, \tag{S33}$$

and $f_\epsilon(\epsilon)$ is the electron energy distribution function, normalised as $\int_0^\infty f_\epsilon(\epsilon)\sqrt{\epsilon}\mathrm{d}\epsilon = 1$. In this work, as in [17–19], we assume that $f_\epsilon(\epsilon)$ is Maxwellian, which reflects the high collisionality of atmospheric pressure discharges [16, 20].

Finally, ϵ_0 in Eq. (S32) is the threshold electron energy. This value can be retrieved from databases, alongside with the cross sections σ_j of elastic ($\Delta\epsilon_j = 0$) or inelastic ($\Delta\epsilon_j < 0$) collisions.

The cross sections of superelastic ($\Delta\epsilon_j > 0$) collisions are calculated by the principle of detailed balance:

$$\sigma_{j,\mathrm{inv}}(\epsilon) = \frac{g_{\mathrm{low}}}{g_{\mathrm{upp}}} \cdot \frac{\epsilon + \Delta\epsilon_j}{\epsilon} \cdot \sigma_j(\epsilon + \Delta\epsilon_j). \tag{S34}$$

Here, σ_j is the inelastic cross section obtained from literature, $\sigma_{j,\mathrm{inv}} = \sigma_{j,\mathrm{inv}}(\epsilon)$ is the (unknown) superelastic cross section, and g_{upp} and g_{low} are the statistical weights of the upper and the lower energy level of the colliding heavy particle. For well-defined levels, *i.e.*, those of CO, O_2, and atomic species, the statistical weights are reported in the LXCat database (see Tab. S6). Unfortunately, the two electronic excitations of CO_2 given in the database represent groups of individual electronic levels, whose composition is not clearly stated by the original authors [21]. Hence, their statistical weights are unknown and the superelastic collisions from CO_2 electronic states cannot be included [22]. However, in microwave plasmas, electronic excitation of CO_2 is anyway a minor channel, considerably less important than thermal chemistry or charged particle kinetics [13, 23].

S3.1.2 Charged Particle Kinetics

The charged heavy particle kinetics mostly follows the references in [13]. This includes electron–ion recombination reactions, although they formally belong to the electron kinetics as well (see the reactions in Tab. S6). However, for these reactions, the rate coefficients are not calculated from Eq. (S4) due to their weak dependence on the electron energy distribution. Nevertheless, their dependence on the electron temperature is contained in the rate expressions. As a result, the rates of their corresponding reverse processes, *i.e.*, associative ionisation, can be calculated through detailed balance as described below.

Associative ionisation reactions are the main electron source at elevated pressures [13]. Notwithstanding that, the measurements of their rates are scarce. Consequently, the rates of similar reactions are often taken instead, which increases the related uncertainty [13, 24].

Therefore, only the rate of O + O associative ionisation is taken from literature, as it is well known from measurements in air systems [24]. The remaining rate coefficients are calculated through the principle of detailed balance, *i.e.*, as unknown reverse rates to the dissociative recombination of molecular ions (CO^+, ${O_2}^+$, ${C_2}^+$ and ${CO_2}^+$). To perform the balancing, both K_j and $k_{j,\mathrm{forward}}$ in Eq. (11) (main text) are evaluated at $T_e = T$, which is the case in local equilibrium [25]. Therefore, the resultant associative ionisation rate coefficients are an exclusive function of the gas temperature T, which reflects the thermal nature of the process. The list of the associative ionisation reactions involved is given in Tab. S5.

Table S5: List of the electron recombination and associative ionisation rate coefficients included in the global model (excerpt from Tab. S6). T_e is given in eV.

No.	Reaction	k_{forward} ($\mathrm{m^3\ s^{-1}}$)	k_{reverse} ($\mathrm{m^3\ s^{-1}}$)	Ref.
(ER1)	${O_2}^+ + e^- \rightleftharpoons O + O$	$5.17 \times 10^{-15} T_e^{-1} +$ $+1.51 \times 10^{-14} T_e^{-0.7}$	$1.86 \times 10^{-17} \cdot$ $\cdot \exp(-80600/T)$	[26] (forward), [24] (reverse)
(ER2)	$CO^+ + e^- \rightleftharpoons C + O$	$1.57 \times 10^{-13} T_e^{-0.4}$	detailed balance	[27]
(ER3)	${CO_2}^+ + e^- \rightleftharpoons CO + O$	$3.94 \times 10^{-13} T_e^{-0.4}$	detailed balance	[27]
(ER4)	${CO_2}^+ + e^- \rightleftharpoons C + O_2$	$3.94 \times 10^{-13} T_e^{-0.4}$	detailed balance	[27]
(ER5)	${C_2}^+ + e^- \rightleftharpoons C + C$	$1.79 \times 10^{-14} T_e^{-0.5}$	detailed balance	[28]

S3.1.3 Vibrational Kinetics

Finally, the vibrational kinetics is based on the model by [22]. However, as in [29], the densities of vibrational levels are retrieved from partition functions, assuming that the vibrational levels are equilibrated at gas temperature. This strategy circumvents the more costly state-to-state approach applied in [22].

The vibrational reactions in Tab. S6 describe the rate of an electron collision with a vibrational level υ of a heavy particle. Under our conditions, the kinetic concentration of that level, $[\mathrm{M}]_\upsilon$, is calculated as

$$[\mathrm{M}]_\upsilon = [\mathrm{M}] \cdot \frac{g_\upsilon \exp\left(-\frac{E_\upsilon}{k_\mathrm{B}T}\right)}{Q_{\upsilon,\mathrm{M}}(T)}. \tag{S35}$$

[M] is the total concentration of M solved in the model and g_υ are the statistical weights of the υ-th vibrational level with energy E_υ. For diatomics, g_υ universally equals 1; for CO_2 it is the product of populated level degeneracies. E_υ is calculated by the harmonic approximation as

$$E_\upsilon = \sum_{m=\text{vibrational modes}} \left(\upsilon_m + \frac{1}{2}\right) h\tilde{c}_0\tilde{\nu}_m. \tag{S36}$$

$h = 6.626 \times 10^{-34}$ J s is the Planck constant, $\tilde{c}_0$ is the vacuum light velocity in cm s^{-1}, and $\tilde{\nu}$ are the fundamental wavenumbers noted in Tab. S4.

Finally, Q_υ in Eq. (S35) is the vibrational partition function. Taking the harmonic approximation results in

$$Q_\upsilon = \prod_{m=\text{vibrational modes}} \frac{1}{1-\exp\left(-\frac{h\tilde{c}_0\tilde{\nu}_m}{k_\mathrm{B}T}\right)}. \tag{S37}$$

Eventually, therefore, the electron-impact excitation of the vibrational level M_υ ($\mathrm{M} = CO_2$, CO, O_2) is described by a rate r_υ of

$$r_\upsilon = k_{j\upsilon} N_e [\mathrm{M}] \cdot \frac{g_\upsilon \exp\left(-\frac{E_\upsilon}{k_\mathrm{B}T}\right)}{Q_{\upsilon,\mathrm{M}}(T)}. \tag{S38}$$

$k_{j\upsilon}$ is the rate coefficient computed by Eq. (S32) for the cross section associated to the υ-th vibrational level. The cross section data are referenced in Tab. S6, together with all reactions mentioned above. For completeness, the neutral heavy particle reactions are copied from Tab. 1, main text.

Table S6: List of chemical reactions involved in the global model.

Elastic electron collisions

No.	Reaction	k (m^3 s^{-1})	Ref.
(E1)	$CO_2 + e^- \longrightarrow CO_2 + e^-$	integrated cross section	[30]
(E2)	$CO + e^- \longrightarrow CO + e^-$	integrated cross section	[31]
(E3)	$O_2 + e^- \longrightarrow O_2 + e^-$	integrated cross section	[31]
(E4)	$O + e^- \longrightarrow O + e^-$	integrated cross section	[32]
(E5)	$C + e^- \longrightarrow C + e^-$	integrated cross section	[32]

Electron-impact (de-)excitation

No.	Reaction	k_{forward} (m^3 s^{-1})	k_{reverse} (m^3 s^{-1})	Ref.
(E6)	$CO_2 + e^- \longrightarrow CO_2(A) + e^-$	integrated cross section	not available	[21]
(E7)	$CO_2 + e^- \longrightarrow CO_2(B) + e^-$	integrated cross section	not available	[21]
(E8)	$CO + e^- \longleftrightarrow CO(a^3\Pi) + e^-$	integrated cross section	detailed balance	[32]
(E9)	$CO + e^- \longleftrightarrow CO(a'^3\Sigma^+) + e^-$	integrated cross section	detailed balance	[32]
(E10)	$O_2 + e^- \longleftrightarrow O_2(^1\Delta_g) + e^-$	integrated cross section	detailed balance	[30]
(E11)	$O_2 + e^- \longleftrightarrow O_2(^1\Sigma_g{}^+) + e^-$	integrated cross section	detailed balance	[30]
(E12)	$O + e^- \longleftrightarrow O(^1D) + e^-$	integrated cross section	detailed balance	[33]
(E13)	$O + e^- \longleftrightarrow O(^1S) + e^-$	integrated cross section	detailed balance	[33]
(E14)	$C + e^- \longleftrightarrow C(^1D) + e^-$	integrated cross section	detailed balance	[34]
(E15)	$C + e^- \longleftrightarrow C(^1S) + e^-$	integrated cross section	detailed balance	[34]

Electron-impact dissociation

No.	Reaction	k (m^3 s^{-1})	Ref.
(E16)	$CO_2 + e^- \longrightarrow CO(a^3\Pi) + O + e^-$	integrated cross section	[35]
(E17)	$CO_2 + e^- \longrightarrow CO + O(^1D) + e^-$	integrated cross section	[35]
(E18)	$CO_2 + e^- \longrightarrow CO + O(^1S) + e^-$	integrated cross section	[35]
(E19)	$CO + e^- \longrightarrow C + O + e^-$	integrated cross section	[36]
(E20)	$O_2 + e^- \longrightarrow O + O + e^-$	integrated cross section	[37]

Electron-impact ionisation

No.	Reaction	k (m^3 s^{-1})	Ref.
(E21)	$CO_2 + e^- \longrightarrow CO_2{}^+ + e^- + e^-$	integrated cross section	[38]
(E22)	$CO_2 + e^- \longrightarrow CO + O^+ + e^- + e^-$	integrated cross section	[38]
(E23)	$CO_2{}^+ + e^- \longrightarrow CO^+ + O + e^- + e^-$	integrated cross section	[38]
(E24)	$CO_2 + e^- \longrightarrow O_2 + C^+ + e^- + e^-$	integrated cross section	[38]
(E25)	$CO + e^- \longrightarrow CO^+ + e^- + e^-$	integrated cross section	[31]
(E26)	$CO + e^- \longrightarrow O + C^+ + e^- + e^-$	integrated cross section	[31]
(E27)	$CO + e^- \longrightarrow C + O^+ + e^- + e^-$	integrated cross section	[31]
(E28)	$O_2 + e^- \longrightarrow O_2{}^+ + e^- + e^-$	integrated cross section	[31]
(E29)	$O_2 + e^- \longrightarrow O + O^+ + e^-$	integrated cross section	[31]
(E30)	$O + e^- \longrightarrow O^+ + e^- + e^-$	integrated cross section	[33]
(E31)	$C + e^- \longrightarrow C^+ + e^- + e^-$	integrated cross section	[34]

Charged heavy particle kinetics

No.	Reaction	k (m^{-3} s^{-1})	Ref.
(C1)	$CO_2 + O^+ \longrightarrow CO + O_2{}^+$	4.5×10^{-16}	[27]
(C2)	$CO_2 + O^+ \longrightarrow O + CO_2{}^+$	4.5×10^{-16}	[27]
(C3)	$CO_2 + C^+ \longrightarrow CO + CO^+$	1.1×10^{-15}	[27]
(C4)	$CO_2 + CO^+ \longrightarrow CO + CO_2{}^+$	1.0×10^{-15}	[27]
(C5)	$CO + O^+ \longrightarrow O + CO^+$	$2.83 \times 10^{-19} T^{0.5} \exp(-4580/T)$	[39]
(C6)	$CO + C^+ \longrightarrow C + CO^+$	5.0×10^{-19}	[39]
(C7)	$C + CO^+ \longrightarrow CO + C^+$	1.1×10^{-16}	[40]
(C8)	$C + O_2{}^+ \longrightarrow O + CO^+$	5.2×10^{-17}	[40]

Charged heavy particle kinetics (continued)

No.	Reaction	k**	Ref.
(C9)	$\mathrm{C} + \mathrm{O_2}^+ \longrightarrow \mathrm{O_2} + \mathrm{C}^+$	5.2×10^{-17}	[40]
(C10)	$\mathrm{O} + \mathrm{CO_2}^+ \longrightarrow \mathrm{CO} + \mathrm{O_2}^+$	1.64×10^{-16}	[40]
(C11)	$\mathrm{O} + \mathrm{CO_2}^+ \longrightarrow \mathrm{CO_2} + \mathrm{O}^+$	9.62×10^{-17}	[40]
(C12)	$\mathrm{O_2} + \mathrm{CO_2}^+ \longrightarrow \mathrm{CO_2} + \mathrm{O_2}^+$	6.4×10^{-17}	[27]
(C13)	$\mathrm{O} + \mathrm{CO}^+ \longrightarrow \mathrm{CO} + \mathrm{O}^+$	1.4×10^{-16}	[27]
(C14)	$\mathrm{O_2} + \mathrm{CO}^+ \longrightarrow \mathrm{CO} + \mathrm{O_2}^+$	1.2×10^{-16}	[27]
(C15)	$\mathrm{O_2} + \mathrm{C}^+ \longrightarrow \mathrm{CO} + \mathrm{O}^+$	6.14×10^{-16}	[27]
(C16)	$\mathrm{O_2} + \mathrm{C}^+ \longrightarrow \mathrm{O} + \mathrm{CO}^+$	3.8×10^{-16}	[27]
(C17)	$\mathrm{O_2} + \mathrm{O}^+ \longrightarrow \mathrm{O} + \mathrm{O_2}^+$	$3.29 \times 10^{-16} T^{-0.5}$	[27]
(C18)	$\mathrm{O} + \mathrm{O}^+ + \mathrm{M} \longrightarrow \mathrm{O_2}^+ + \mathrm{M}^*$	1.0×10^{-35}	[41]
(C19)	$\mathrm{O} + \mathrm{O_2}^+ \longrightarrow \mathrm{O_2} + \mathrm{O}^+$	$6.64 \times 10^{-18} T^{-0.09} \exp(-18000/T)$	[24]
(C20)	$\mathrm{O_2} + \mathrm{C}^+ \longrightarrow \mathrm{C} + \mathrm{O_2}^+$	$1.66 \times 10^{-17} \exp(-9400/T)$	[24]
(C21)	$\mathrm{CO_2} + \mathrm{e}^- \longrightarrow \mathrm{C} + \mathrm{O_2}^+ + \mathrm{e}^-$	$7.0 \times 10^{-19} T_e^{0.5} (1 + 1.3 \times 10^{-5} T_e) \cdot$ $\cdot \exp(-150000/T_e)$	[27]
(C22)	$\mathrm{O_2}^+ + \mathrm{e}^- + \mathrm{M} \longrightarrow \mathrm{O} + \mathrm{O} + \mathrm{M}$	$1.61 \times 10^{-33} T_e^{-0.5}$	[27]
(C23)	$\mathrm{O}^+ + \mathrm{e}^- + \mathrm{M} \longrightarrow \mathrm{O} + \mathrm{M}$	$2.49 \times 10^{-35} T_e^{-1.5}$	[41]

* M = any neutral   ** $\mathrm{m^3\ s^{-1}}$ (2nd order); $\mathrm{m^6\ s^{-1}}$ (3rd order)

T is given in K. T_e is given in eV, except for reaction (C21) where T_e is in K.

Electron-ion recombination and associative ionisation

No.	Reaction	k_{forward} ($\mathrm{m^3\ s^{-1}}$)	k_{reverse} ($\mathrm{m^3\ s^{-1}}$)	Ref.
(ER1)	$\mathrm{O_2}^+ + \mathrm{e}^- \rightleftharpoons \mathrm{O} + \mathrm{O}$	$5.17 \times 10^{-15} T_e^{-1} +$ $+ 1.51 \times 10^{-14} T_e^{-0.7}$	$1.86 \times 10^{-17} \cdot$ $\cdot \exp(-80600/T)$	[26] (forward), [24] (reverse)
(ER2)	$\mathrm{CO}^+ + \mathrm{e}^- \rightleftharpoons \mathrm{C} + \mathrm{O}$	$1.57 \times 10^{-13} T_e^{-0.4}$	detailed balance	[27]
(ER3)	$\mathrm{CO_2}^+ + \mathrm{e}^- \rightleftharpoons \mathrm{CO} + \mathrm{O}$	$3.94 \times 10^{-13} T_e^{-0.4}$	detailed balance	[27]
(ER4)	$\mathrm{CO_2}^+ + \mathrm{e}^- \rightleftharpoons \mathrm{C} + \mathrm{O_2}$	$3.94 \times 10^{-13} T_e^{-0.4}$	detailed balance	[27]
(ER5)	$\mathrm{C_2}^+ + \mathrm{e}^- \rightleftharpoons \mathrm{C} + \mathrm{C}$	$1.79 \times 10^{-14} T_e^{-0.5}$	detailed balance	[28]

T_e is given in eV.

Neutral heavy particle kinetics

No.	Reaction	k_{forward}**	k_{reverse}**	Ref.
(N1)	$\mathrm{CO} + \mathrm{O} + \mathrm{M} \rightleftharpoons \mathrm{CO_2} + \mathrm{M}^*$	Lindemann falloff	detailed balance	[42]
(N2)	$\mathrm{C} + \mathrm{O} + \mathrm{M} \rightleftharpoons \mathrm{CO} + \mathrm{M}$	$9.12 \times 10^{-34} T^{-3.08} \cdot$ $\cdot \exp(-2114.0/T)$	detailed balance	[43]
(N3)	$\mathrm{C_2} + \mathrm{M} \rightleftharpoons \mathrm{C} + \mathrm{C} + \mathrm{M}$	$2.49 \times 10^{-14} \cdot$ $\cdot \exp(-71562.1/T)$	detailed balance	[44]
(N4)	$\mathrm{O} + \mathrm{O} + \mathrm{CO_2} \rightleftharpoons \mathrm{O_2} + \mathrm{CO_2}$	$1.19 \times 10^{-42} T^{-1}$	detailed balance	[42]
	$\mathrm{O} + \mathrm{O} + \mathrm{CO} \rightleftharpoons \mathrm{O_2} + \mathrm{CO}$	$5.79 \times 10^{-43} T^{-1}$	detailed balance	[42]
	$\mathrm{O} + \mathrm{O} + \mathrm{M} \rightleftharpoons \mathrm{O_2} + \mathrm{M}$ $\mathrm{M} \neq \mathrm{CO}, \mathrm{CO_2}$	$3.31 \times 10^{-43} T^{-1}$	detailed balance	[42]
(N5)	$\mathrm{CO} + \mathrm{O_2} \rightleftharpoons \mathrm{CO_2} + \mathrm{O}$	$4.15 \times 10^{-18} \cdot$ $\cdot \exp(-24070.0/T)$	detailed balance	[42]
(N6)	$\mathrm{C} + \mathrm{O_2} \rightleftharpoons \mathrm{CO} + \mathrm{O}$	$9.63 \times 10^{-17} \cdot$ $\cdot \exp(-290.05/T)$	detailed balance	[42]

* M = any neutral   ** $\mathrm{m^3\ s^{-1}}$ (2nd order); $\mathrm{m^6\ s^{-1}}$ (3rd order)

T is given in K.

Vibrational kinetics

No.	Reaction	k_{forward} ($\text{m}^3\ \text{s}^{-1}$)	k_{reverse} ($\text{m}^3\ \text{s}^{-1}$)	Ref.
(V1)	$CO_2 + e^- \longleftrightarrow CO_2(010) + e^-$	integrated cross section	detailed balance	[30]
(V2)	$CO_2 + e^- \longleftrightarrow CO_2(020) + e^-$	integrated cross section	detailed balance	[30]
(V3)	$CO_2 + e^- \longleftrightarrow CO_2(030) + e^-$	integrated cross section	detailed balance	[30]
(V4)	$CO_2 + e^- \longleftrightarrow CO_2(040) + e^-$	integrated cross section	detailed balance	[30]
(V5)	$CO_2 + e^- \longleftrightarrow CO_2(050) + e^-$	integrated cross section	detailed balance	[30]
(V6)	$CO_2 + e^- \longleftrightarrow CO_2(100) + e^-$	integrated cross section	detailed balance	[30]
(V7)	$CO_2 + e^- \longleftrightarrow CO_2(200) + e^-$	integrated cross section	detailed balance	[30]
(V8)	$CO_2 + e^- \longleftrightarrow CO_2(300) + e^-$	integrated cross section	detailed balance	[30]
(V9)	$CO_2 + e^- \longleftrightarrow CO_2(001) + e^-$	integrated cross section	detailed balance	[30]
(V10)	$CO_2 + e^- \longleftrightarrow CO_2(002) + e^-$	integrated cross section	detailed balance	[30]
(V11)	$CO_2 + e^- \longleftrightarrow CO_2(003) + e^-$	integrated cross section	detailed balance	[30]
(V12)	$CO_2 + e^- \longleftrightarrow CO_2(004) + e^-$	integrated cross section	detailed balance	[30]
(V13)	$CO_2 + e^- \longleftrightarrow CO_2(005) + e^-$	integrated cross section	detailed balance	[30]
(V14)	$CO_2 + e^- \longleftrightarrow CO_2(110) + e^-$	integrated cross section	detailed balance	[30]
(V15)	$CO_2 + e^- \longleftrightarrow CO_2(120) + e^-$	integrated cross section	detailed balance	[30]
(V16)	$CO_2 + e^- \longleftrightarrow CO_2(130) + e^-$	integrated cross section	detailed balance	[30]
(V17)	$CO_2 + e^- \longleftrightarrow CO_2(011) + e^-$	integrated cross section	detailed balance	[30]
(V18)	$CO_2 + e^- \longleftrightarrow CO_2(021) + e^-$	integrated cross section	detailed balance	[30]
(V19)	$CO_2 + e^- \longleftrightarrow CO_2(101) + e^-$	integrated cross section	detailed balance	[30]
(V20)	$CO_2 + e^- \longleftrightarrow CO_2(110) + e^-$	integrated cross section	detailed balance	[30]
(V21)	$CO_2 + e^- \longleftrightarrow CO_2(120) + e^-$	integrated cross section	detailed balance	[30]
(V22)	$CO_2 + e^- \longleftrightarrow CO_2(210) + e^-$	integrated cross section	detailed balance	[30]
(V23)	$CO + e^- \longleftrightarrow CO(\upsilon = 1)$	integrated cross section	detailed balance	[45]
(V24)	$CO + e^- \longleftrightarrow CO(\upsilon = 2)$	integrated cross section	detailed balance	[45]
(V25)	$CO + e^- \longleftrightarrow CO(\upsilon = 3)$	integrated cross section	detailed balance	[45]
(V26)	$CO + e^- \longleftrightarrow CO(\upsilon = 4)$	integrated cross section	detailed balance	[45]
(V27)	$CO + e^- \longleftrightarrow CO(\upsilon = 5)$	integrated cross section	detailed balance	[45]
(V28)	$CO + e^- \longleftrightarrow CO(\upsilon = 6)$	integrated cross section	detailed balance	[45]
(V29)	$CO + e^- \longleftrightarrow CO(\upsilon = 7)$	integrated cross section	detailed balance	[45]
(V30)	$CO + e^- \longleftrightarrow CO(\upsilon = 8)$	integrated cross section	detailed balance	[45]
(V31)	$CO + e^- \longleftrightarrow CO(\upsilon = 9)$	integrated cross section	detailed balance	[45]
(V32)	$CO + e^- \longleftrightarrow CO(\upsilon = 10)$	integrated cross section	detailed balance	[45]
(V33)	$O_2 + e^- \longleftrightarrow O_2(\upsilon = 1)$	integrated cross section	detailed balance	[30]
(V34)	$O_2 + e^- \longleftrightarrow O_2(\upsilon = 2)$	integrated cross section	detailed balance	[30]
(V35)	$O_2 + e^- \longleftrightarrow O_2(\upsilon = 3)$	integrated cross section	detailed balance	[30]
(V36)	$O_2 + e^- \longleftrightarrow O_2(\upsilon = 4)$	integrated cross section	detailed balance	[30]

S3.2 Electrical Conductivity

Solving the global model in steady state yields the electron density and electron momentum frequency as functions of T and $\dot{q}_{\mathrm{rh}}$ for the constant pressure of 930 mbar. Their values are illustrated in Fig. S5.

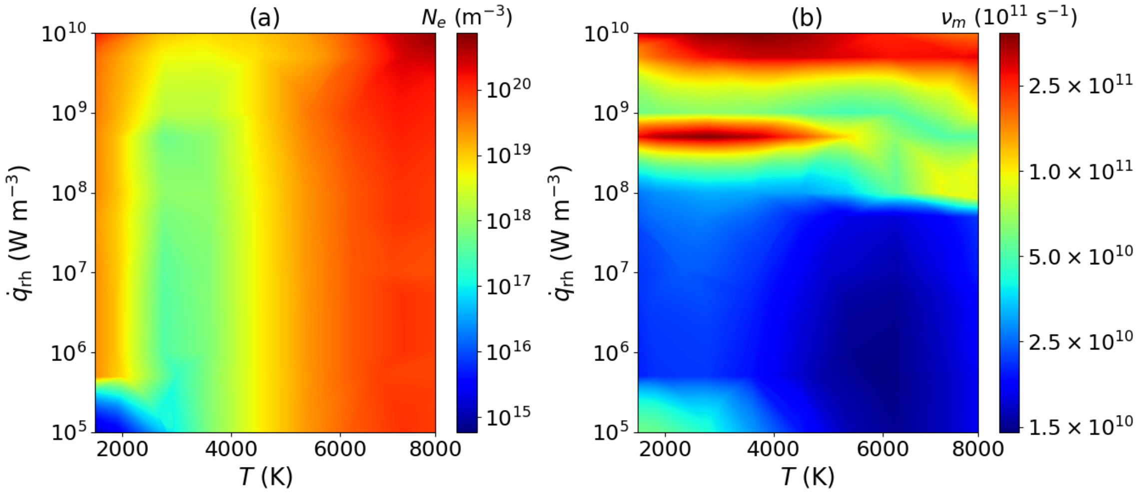

Figure S5: Electron density (a) and electron momentum frequency (b) plotted as functions of gas temperature and microwave heat rate.

The electron density increases with both T and $\dot{q}_{\mathrm{rh}}$, which is a logical observation. Above ~3000 K, N_e is in good order-of-magnitude agreement with the values obtained in [13] by Thomson scattering of contracted discharges. Below 3000 K, experimental data are scarcer and more difficult to interpret [46], and the Maxwellian approximation is more prone to inaccuracies as well [11]. In contracted discharges, however, microwave power absorption in this temperature region is insignificant [11, 47, 48]. For $T \in [2000\text{ K}; 3000\text{ K}]$, most N_e values in Fig. S5(a) are close to, or lower than the collisionless critical density of a 2.45 GHz discharge ($\sim 10^{17}$ m^{-3}). At atmospheric conditions, moreover, the discharge is highly collisional ($\nu_m \gg \omega_s$; [49]) and yet higher electron densities are therefore required for efficient power coupling [48]. In our case, this corresponds to the temperatures of $\gtrsim$ 4000 K observed at the edge of the plasma (*e.g.*, Fig. 12, main text). Regions on the farther periphery (T = 2000–3000 K or lower) are therefore unlikely to sustain a sufficient power absorption and influence our multidimensional model. We believe that this assumption holds despite some enhancement of the N_e values below 2000 K seen in Fig. S5(a).

Finally, at constant pressure, increasing N_e introduces a decrease in the number density of heavy particles and consequently also in the electron–neutral collision frequency. As a result, ν_m in Fig. S5(b) generally decreases with increased temperature. Conversely, ν_m increases with increasing $\dot{q}_{\mathrm{rh}}$, *i.e.*, with higher energy delivered to the electrons. These effects combine into a maximum observed for $\dot{q}_{\mathrm{rh}} \sim 10^9$ W m^{-3} and $T \in [1000\text{ K}; 4000\text{ K}]$. Above 10^9 W m^{-3}, the trend in ν_m changes and another maximum is observed at $\sim 10^{10}$ W m^{-3}. We currently do not have a full explanation for this kinetic phenomenon. However, it is possible that the Maxwellian approximation is insufficient for the region of $[1000\text{ K}; 4000\text{ K}] \times [10^9\text{ W m}^{-3}; 10^{10}\text{ W m}^{-3}]$ and the local minimum observed there is an artifact. In the future, this can be confirmed by solving the global model with a non-Maxwellian EEDF. However, as discussed above, the region in question does not sustain microwave power in multidimension, and therefore does not introduce an uncertainty of concern.

Formally, the results in Fig. S5 correspond to a non-isothermal system. This is illustrated in Fig. S6 by plotting the ratio of electron and gas temperature (T_e/T).

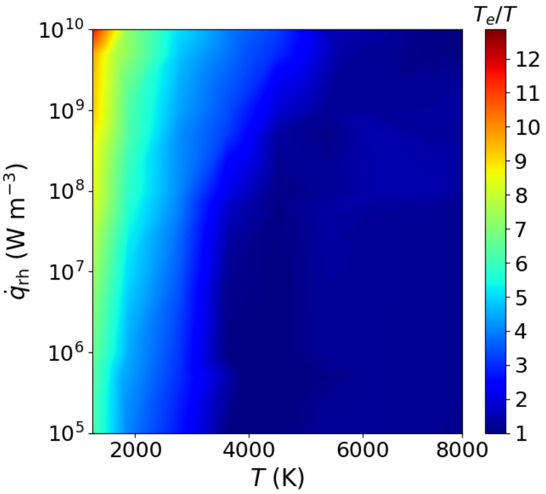

Figure S6: T_e/T ratio plotted as a function of gas temperature and the microwave heat rate.

As shown in the figure, T_e is generally higher than T, and the two temperatures limit to each other at $T \gtrsim 5000$ K. These observations are consistent with the fundamental description of microwave plasma [50]. The values of $T_e > 10T$ at $\sim 10^9$–10^{10} W m^{-3} might be an artifact coming from the Maxwellian EEDF [46] and are likely linked to the varying trend in ν_m discussed above. However, as indicated, microwave power deposition in this region is unlikely [47]. For the remaining conditions, both the trend and values of T_e are reasonable.

The non-isothermality of the system confirms the importance of the two-temperature approach to calculating the reaction rates in Tab. S6. In the future, enhanced computational resources can further improve our approach by including Tab. S6 in a multidimensional model and calculating T_e self-consistently. At this stage, T_e influences the fluid model implicitly *via* N_e and ν_m, which already seems to be a reasonable description of atmospheric pressure experiments.

S4 Electromagnetics

S4.1 Mesh Independence Study

The electromagnetic field simulations start with testing the mesh partitioning of the resonator cavity. As in Sec. S1.2.1, the mesh sizes are gradually refined within the test, starting with the default COMSOL settings for a frequency domain electromagnetic simulation. The simulation outcomes are evaluated by recording the port scattering parameter, as listed in Tab. S7. The test is conducted without plasma.

Table S7: Results of the mesh independence study involving the electromagnetic calculations.

Mesh size (mm)	$-\log_{10}(S)$ (dB)	CPU time
1.4–6	−0.03955	60 s
1–4	−0.03954	60 s
0.8–3	−0.03954	60 s
0.2–2.4	−0.03954	60 s

As anticipated by [51] and references therein, the calculation is practically insensitive to refining the mesh elements smaller than $\frac{\lambda}{10} \doteq 12$ mm for the vacuum wavelength of $\frac{c_0}{2.45\times10^9\ \mathrm{Hz}}$. For subsequent calculations, the second entry in Tab. S7 is arbitrarily chosen, which makes the mesh one level finer than the one used in COMSOL tutorial textbooks [52].

S4.2 Electric Field Without Plasma

The mesh independence study results in calculating the E field profile without the plasma discharge, as exemplified in Fig. S7.

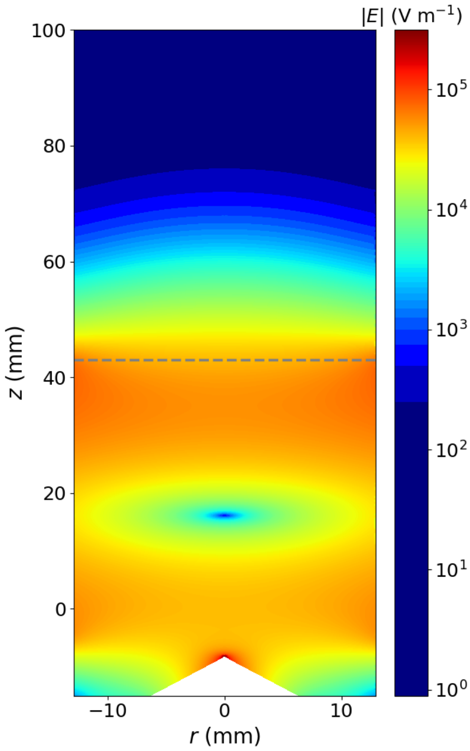

Figure S7: Electric field amplitude calculated without plasma.

The field sustains a standing wave in the cavity and is significantly enhanced at the tip of the coaxial resonator, as expected according to [53]. Due to the geometry of the cavity, $|E| \cong |E_z|$.

S4.3 Minimisation of the Scattering Parameter

Next, the microwave field is coupled to heat transfer in the reactor (Sec. 2.4, main text), for which we explore the resonance conditions in our geometry. The resonant frequency of a cylindrical cavity is generally written as

$$\nu = \frac{1}{2\pi} \cdot \frac{c_0}{\sqrt{\mu_R \varepsilon_R}} g(r) \; [54] \tag{S39}$$

where g is a function of geometry, *i.e.*, in our case, of radius. Since $\mu_R = 1$ and the geometry is fixed by our description of the experiment, we mimic the resonance tuning by altering the dielectric constant ε_R inside the resonator. Resonance is then taken as the state that minimises the port scattering parameter and hence the reflected power. The test is done while solving the microwave field on top of a background heat source (see Sec. 2.4, main text) but its results remain the same throughout the whole model coupling. The minimisation of S is illustrated in Fig. S8.

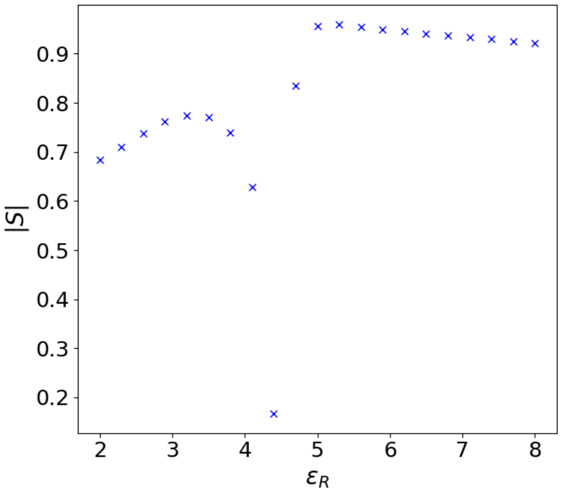

Figure S8: The magnitude of the port scattering parameter plotted as a function of the relative permittivity in the resonator.

The figure shows a sharp minimum whose shape resembles an output of a real port network analyser [51]. Maintaining $\varepsilon_R = 4.5$ then provides sufficient coupling efficiency throughout all condition scans in the main text.

S4.4 Electric Field With Plasma

The fluid–electromagnetic coupling defines the discharge and changes the properties of the propagating wave, as discussed in Sec. 3.1.4, main text. For completeness, we complement the E field analysis in Fig. 10 (main text) in the remaining cut lines, *i.e.*, $E_z(r)$ and $E_r(z)$, respectively. The cut-line plots for 900 W and 2700 W of deposited power at 10 SLM are shown in Fig. S9.

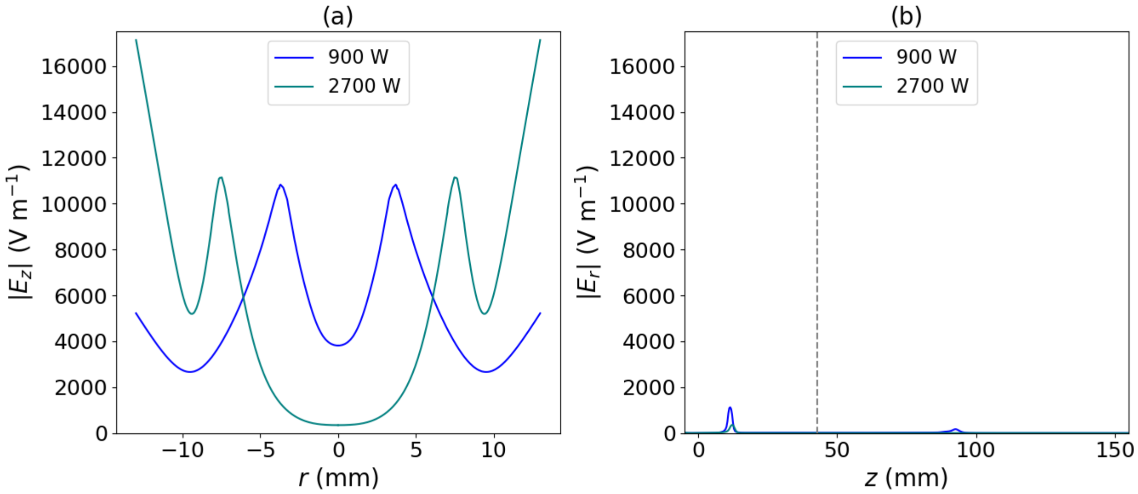

Figure S9: Axial (a) and radial (b) components of the E field calculated for 900 W (blue) and 2700 W (green) of deposited power at 10 SLM. The choice of cut lines corresponds to Fig. 10, main text, and the end of the microwave resonator in panel (b) is marked by a dotted line.

$E_z(r)$ features sharp local maxima at the discharge edges, beyond which the field is again lowered. The position of the maxima coincides with the cusps in Fig. 10(a), main text. However, the interpretation of this plot might be more complicated than in the main text, because additional local minima appear in $E_z(r)$ due to its nodal structure.

$E_r(z)$ in Fig. S9(b), moreover, is not practical for further interpretation. Although the figure shows certain enhancement at the axial edges of the discharge, its peak values, if compared to Fig. 10 (main text) or Fig. S9(a), are barely discernible. This happens due to the near-complete depletion of E_r in the centre of the discharge as discussed in the main text. Because of that, the choice of $E_r(r)$ and $E_z(z)$ for the field analysis in Sec. 3.1.4, main text, is the most convenient combination.

Besides the temperature profiles shown in the main text, the E field is also related to the electron density distribution in the system. This is illustrated in Fig. S10 which superimposes the E field profiles from Fig. 12 (main text) over the corresponding electron density distributions.

As in Fig. 12, main text, the E field peaks in Fig. S10 are aligned with the inflection points in both $N_e(r)$ (Fig. S10(a)) and $N_e(z)$ (Fig. S10(b)). In [46], the inflection point in $N_e(r)$ is used as an indication of discharge contraction, which we capture even at elevated power where the electron density exhibits a very flat core.

Hence, according to our simulations, T and N_e can be interchangeably used to define the size of the contracted discharge in a clear relation to the microwave field that sustains it. Due to this relation, we recommend measuring the discharge size using its temperature or electron density, as opposed to the light emission profiles that have been found uncertain [55]. This recommendation is further justified by estimating the skin depth of the modelled discharges.

The skin depth of a conductor is defined as

$$\delta_s = \frac{1}{\mathfrak{Re}(\sqrt{\mathbf{i}\omega_s \mu_0 \sigma})}\ [54], \tag{S40}$$

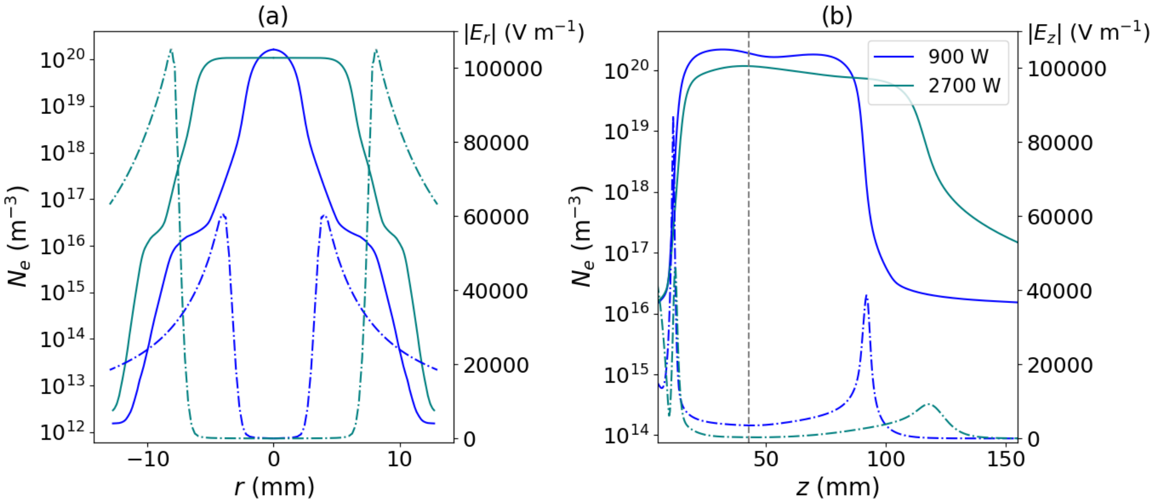

Figure S10: Radial (a) and axial (b) profiles of electron density (solid) and electric fields (dash-dotted; secondary axes). $P = 900$ W (blue) and 2700 W (green), $\phi = 10$ SLM.

in which σ is the electrical conductivity, defined under our approximations by Eq. (19), main text.

In Fig. S11, two example radial profiles of δ_s are superimposed over $E_r(r)$ taken from Fig. 10(a), main text.

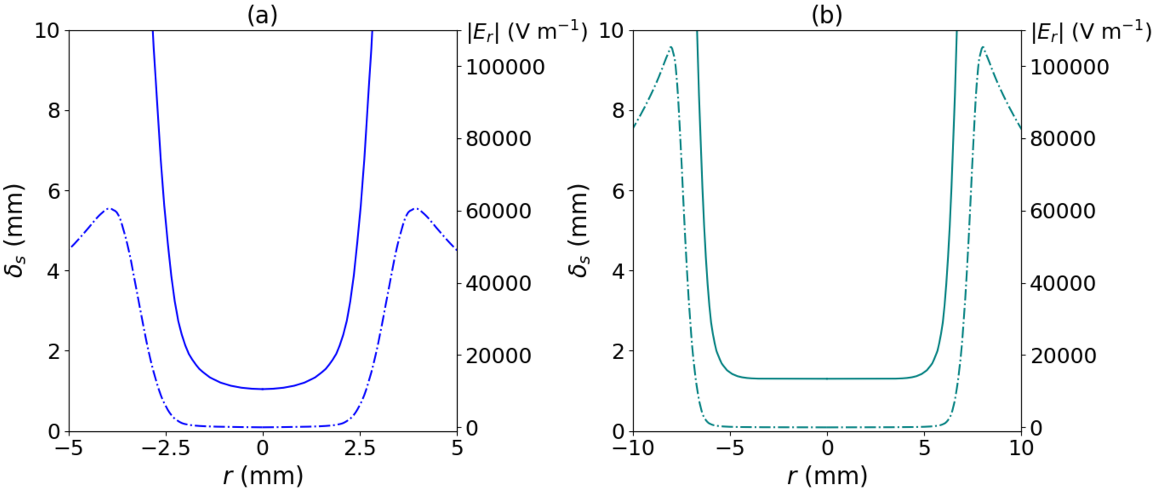

Figure S11: Radial profiles of skin depth (solid) and $|E_r|$ (dash-dotted; secondary axes) for 900 W (blue; a) and 2700 W (green; b) of deposited power at 10 SLM. A different scale of the x axes is chosen for graphical clarity.

As indicated, the $|E_r|$ cusps (*i.e.*, discharge edges) correspond to the regions where δ_s increases above 10 mm, *i.e.*, one order of magnitude above the near-constant value found around $r = 0$. The near-constant δ_s region can therefore be understood as the core of the discharge.

In the core region, δ_s reaches ∼1.1 mm for 900 W and ∼1.3 mm for 2700 W. These values are close to each other, which signifies similar conductivities of the discharge medium. However, at 900 W, the discharge core is seen up to $r_\mathrm{d} \approx 1.2$ mm, whereas at 2700 W, it extends up to $r_\mathrm{d} \approx 4.0$ mm. At 900 W, therefore, $r_\mathrm{d} \sim \delta_s$, and E field penetrates into the discharge core with significant magnitudes ($\sim 10^4$ V m^{-1} in Fig. 9(a), main text). At comparable SEI, similar E fields in the discharge core were found by a heat source-based electromagnetic simulation in [56].

However, when the discharge broadens with increased power, this observation no longer holds. In Fig. S11(b), $r_d > 3\delta_s$, which corresponds to a near-complete ($> 95\%$; [54]) screening of the incident field (see Fig. 9(b), main text). This behaviour can be used as an alternative explanation of the hollow heat source profile found in Fig. 11(b), main text.

Therefore, the discharge size and its skin depth do not seem *a priori* related as was assumed in [57]. Instead, this section attempts to frame the skin depth profile with the discharge size inferred from its electric field, temperature (Fig. 12, main text), or electron density distribution. It is recognised, however, that the current results are simplified and that a self-consistent treatment of the electrical properties would provide more accurate conclusions.

S5 Plasma Size Estimation

As justified above, our simulations use electron density to define the discharge size, as opposed to light emission imaging used in the experiment [4]. Nevertheless, to make both approaches as comparable as possible, the 2–D axisymmetric N_e profiles are appropriately preprocessed to mimic the experimental data collection. This is described as follows below.
The experimental iCCD signal is collected along two separate lines of sight (LOS), which allows a separate measurement of the plasma diameter and length, respectively. The lines of sight are sketched in Fig. S12.

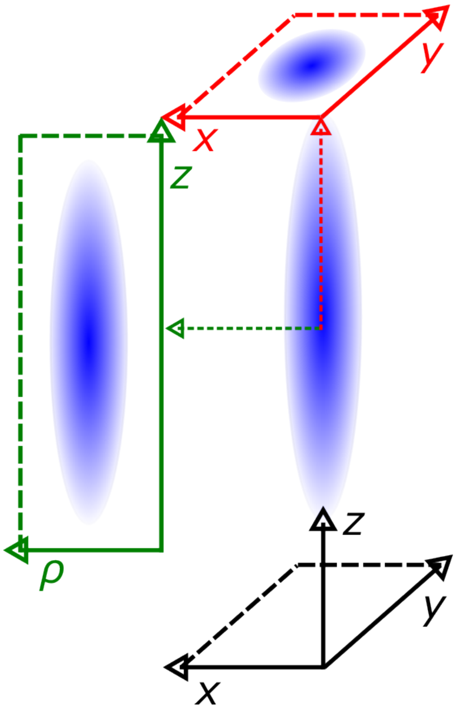

Figure S12: Sketch of the lines of sight (LOS) used for plasma size estimation. The LOS are shown as dotted lines and the different coordinate systems are described further in the text.

In the figure, the plasma is shown as a 3–D object in the Cartesian system (xyz). To measure the plasma diameter, its light emission is axially integrated along the red LOS. This gives a 2–D image (xy) shown on top of the figure. For the length measurement, the 3–D discharge is viewed from side, *i.e.*, along the dark green LOS. This projects the 3–D image onto a 2–D plane (ρz). Finally, the signal is integrated along the ρ-axis in that plane, which [4] denotes by radial integration. A 15% signal threshold is used to define the experimental size in both cases [4].
We simulate the diameter measurement by integrating N_e over the z axis, which gives the following r-dependent integral:

$$\left(\int_z N_e \mathrm{d}z\right)(r) =: \int_{z=0}^{400\text{ mm}} N_e(r,z)\mathrm{d}z. \tag{S41}$$

$\int_z N_e \mathrm{d}z$ is the plotted in the xy plane, with its coordinates defined as

$$x = r(\cos\vartheta); \qquad y = r\sin(\vartheta); \qquad \vartheta \in [0; 2\pi]. \tag{S42}$$

Fig. S13 shows an example of such plots, obtained for 900 W (a) and 2700 W (b) at 10 SLM.

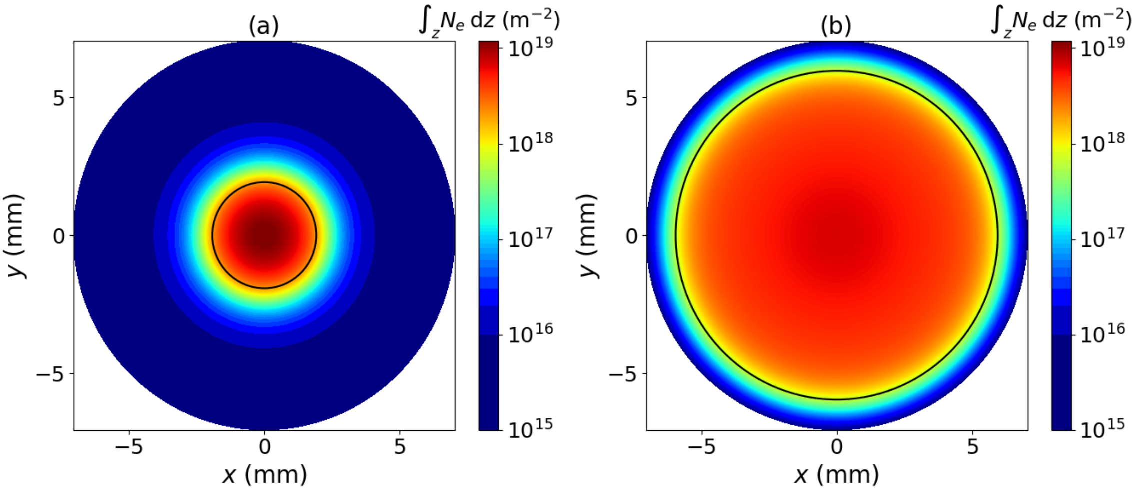

Figure S13: An example of plasma diameter estimation, shown for 900 W (a) and 2700 W (b) of absorbed power at 10 SLM. The diameter at which $\int_z N_e \mathrm{d}z$ reaches 15% of its maximum is marked with a black circle.

The procedure is repeated for all powers in the scanned range, and the resulting diameters are shown in Fig. 8(a), main text.
For the length estimation, the projection in Fig. S12 is provided by a forward Abel transform ($\mathcal{A}(\cdot)$) of our simulated N_e data. The transform is done using the Hansenlaw numerical algorithm [58] implemented in `python-pyabel` [59]. The 15% offset is taken at the ρ-integrated values of the transform, *i.e.*, in shorthand notation, at

$$\left(\int_\rho \mathcal{A}(N_e)\mathrm{d}\rho\right)(z) =: \int_{\rho=0}^{13\ \mathrm{mm}} 2\mathrm{d}\rho \underbrace{\int_\rho^\infty \frac{N_e(r,z)r\mathrm{d}r}{\sqrt{r^2-\rho^2}}}_{\text{Hansenlaw}} . \tag{S43}$$

An example of the final results is shown in Fig. S14.

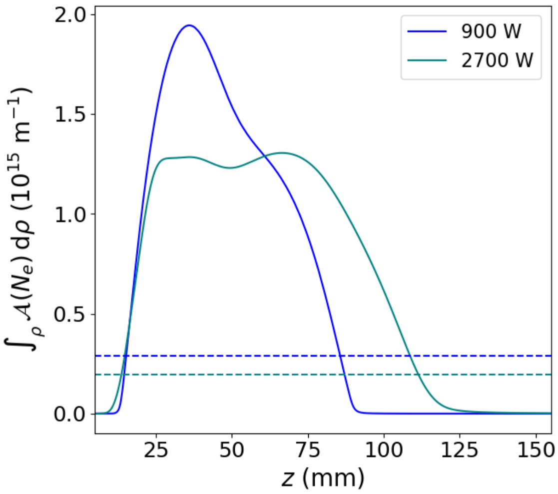

Figure S14: An example of the plasma length estimation, shown for 900 W (blue) and 2700 W (green) of absorbed power at 10 SLM. The 15% offset is marked by dashed lines.

The plasma length is then taken as the position difference of the 2 axial coordinates that correspond to the 15% offset. Its values across the power scan are shown in Fig. 8(b).

S6 Supplementary Mass and Energy Balance Data

Additional mass and energy balance examples in this section complement those in the main text.
First, in Fig. S15, we plot the radial and axial velocities that correspond to the convective transport analysis in Fig. 15, main text ($\phi = 20$ SLM; $P = 2900$ W).

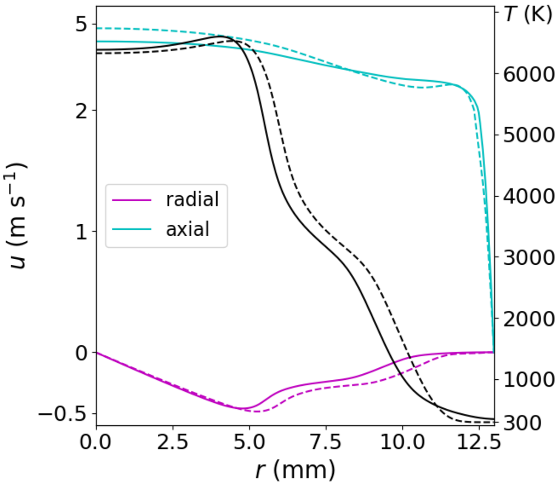

Figure S15: Radial and axial velocities plotted in a radial cut line for $\phi = 20$ SLM and $P = 2900$ W. The secondary axis shows the corresponding gas temperature (black lines). SST data are plotted as solid lines and laminar flow simulations are indicated by dashed lines.

As discussed in the main text, the radial velocities are negative throughout the cut line, whereas axial velocities show significant positive values. Consequently, radial convection transports CO towards the centre of the reactor, while axial convection is directed towards the reactor exhaust.
Another complementary analysis further explores the reactivity of CO molecules along the reactor axis. First, in Fig. S16, we split the reactive source term R_{CO} from Fig. 16 (main text) into its forward (CO formation) and reverse (CO destruction) components.

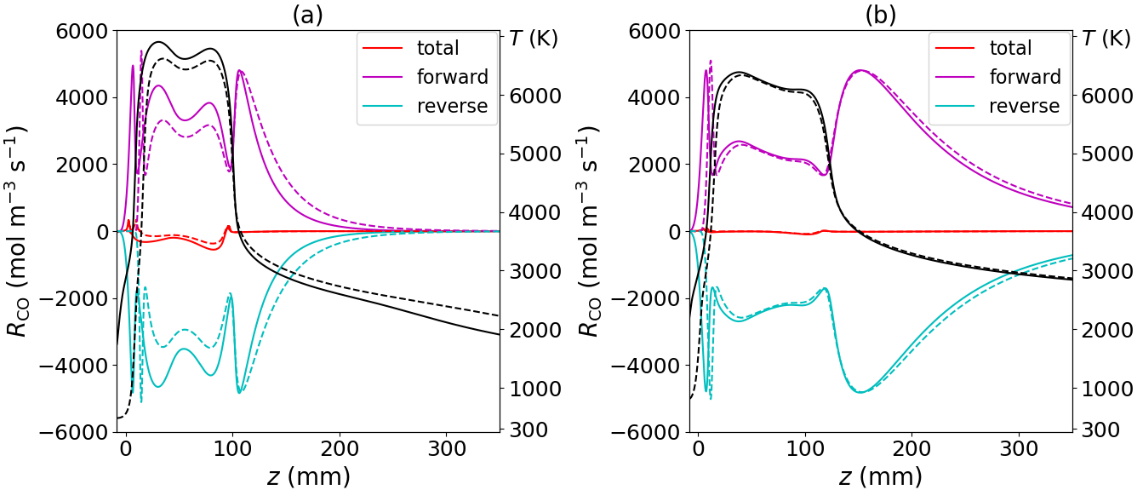

Figure S16: CO reaction rates on the axis of symmetry for $\phi = 20$ SLM and $P = 1100$ W (a) and 2900 W (b). Secondary axes show the corresponding gas temperature (black lines). SST data are plotted as solid lines and laminar flow simulations are indicated by dashed lines.

The forward and reverse rates are defined according to

$$R_{\text{CO}} =: \underbrace{\sum_{j=\text{reactions}} \nu_{\text{CO},j,\text{forward}} r_{j,\text{forward}}}_{R_{\text{CO}},\text{forward}} + \underbrace{\sum_{j=\text{reactions}} -\nu_{\text{CO},j,\text{reverse}} r_{j,\text{reverse}}}_{R_{\text{CO},\text{reverse}}} \tag{S44}$$

in which r_j are the reaction rates taken from Tab. 1, main text. Their individual contributions to R_{CO} are detailed in [60]. Fig. S16 then indicates that both CO production and reoxidation proceed with significant rates outside the plasma ($T < 4500$ K). CO only stops reacting after the gas temperature drops below ∼2500 K, which is only observed in Fig. S16(a). However, due to the elevated temperatures on the reactor axis, the forward and reverse rates end up compensating each other, and no net reactive source is sustained outside the discharge. CO reactivity is thus more important at $|r| > 0$, which is confirmed by showing the 2–D distribution of R_{CO} in Fig. S17.

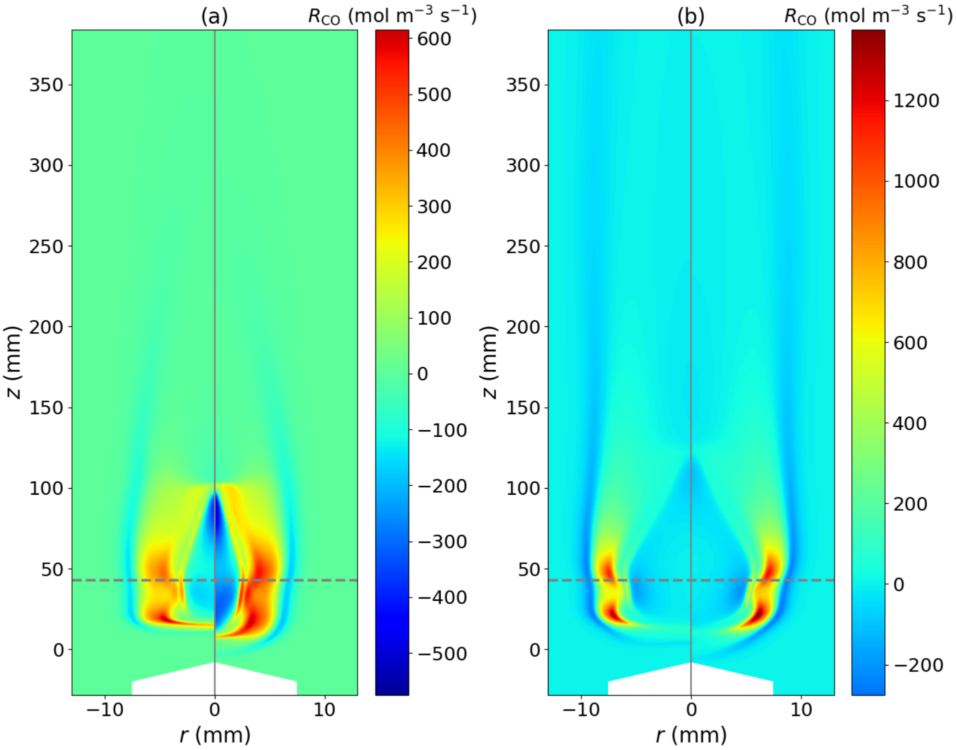

Figure S17: Net reactive rates of CO calculated for $\phi = 20$ SLM and $P = 1100$ W (a) and 2900 W (b) (note the different colour bar scales). In each panel, the results of the laminar flow and SST models are shown in the left-hand side and right-hand side, respectively. The dotted lines indicate the end of the microwave resonator.

The figure shows both the regions of significant CO production discussed in the main text and the near-zero R_{CO} outside the discharge at $r = 0$. Besides that, however, R_{CO} reaches negative values in the effluent gas ($|r| > 0$; $z > 150$–200 mm), which signifies further CO reoxidation in the discharge-heated vortex flow. At elevated power, *i.e.*, in Fig. S17(b), this reactive sink is visible throughout the whole reactor up to the outflow boundary.

This reactive sink is responsible for CO losses outside the plasma, and its presence close to the reactor exhaust further explains the concept of cooling capacity discussed in [61] and in the main text. Furthermore, these results suggest that the radial diffusion of CO from the reactor axis (see Fig. 16) ultimately leads to its reoxidation, which is an undesirable phenomenon. Without additional quenching or cooling mechanisms, diffusion therefore contributes not only to CO_2 conversion but also to product losses in the system. Unlike that, the convective transport at

$r = 0$ is exclusively ($> 98\%$) axial and carries the CO products towards the reactor outflow. In modern CO_2 reactors, this effect is aided by additional flow constrictions, whose modelling will be covered in our future work.

The following figures complete Sec. 3.3–3.4, main text, by showing the mass and energy balance data for the remaining conditions or cut lines. Fig. S18 plots the mass balance data for 40 SLM at $r = 0$.

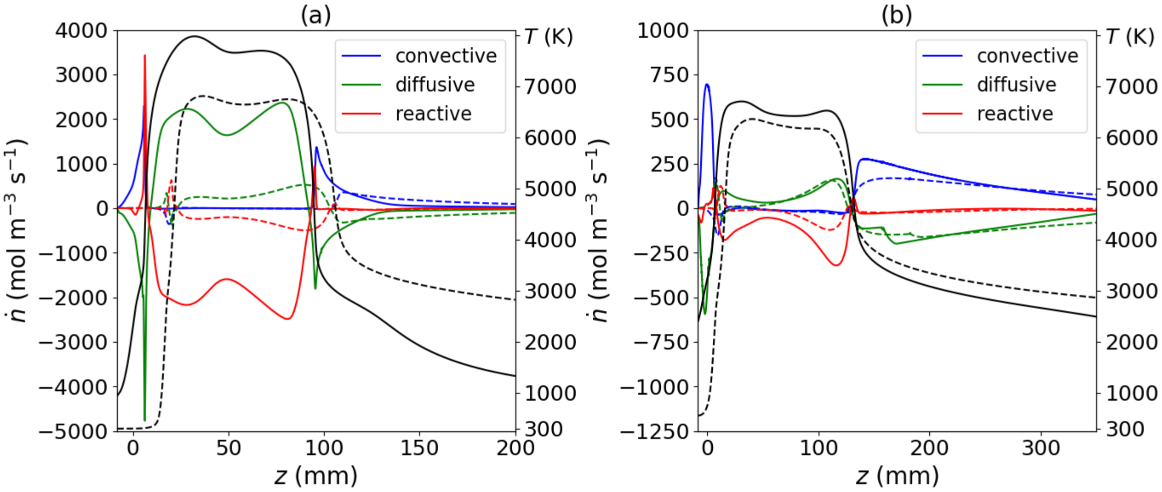

Figure S18: Mass balance of CO solved on the axis of symmetry for $\phi = 40$ SLM and $P = 1100$ W (a) and 2900 W (b). Secondary axes show the corresponding gas temperature (black lines). SST data are plotted as solid lines and laminar flow simulations are indicated by dashed lines. Compare this figure to Fig. 16, main text.

The molar rates behave similarly to Fig. 16, and the difference between laminar and turbulent flow is higher due to the elevated flow rate. The same trend is reflected in the transport coefficients shown in Fig. S19–S20.

Fig. S19 confirms that the biggest difference between the two flow models occurs in the centre of the plasma, *i.e.*, in the region where molecular diffusion dominates [62]. Due to the lower flow rate, moreover, the difference is smaller than for $\phi = 40$ SLM in Fig. 18.

Conversely, the thermal conductivity predicted by the SST model in Fig. S20 is clearly higher in the regions of elevated turbulent kinetic energy (see Fig. 23, main text). As in Fig. 19, this corresponds to the turbulent edges of the discharge, rather than to the plasma itself.

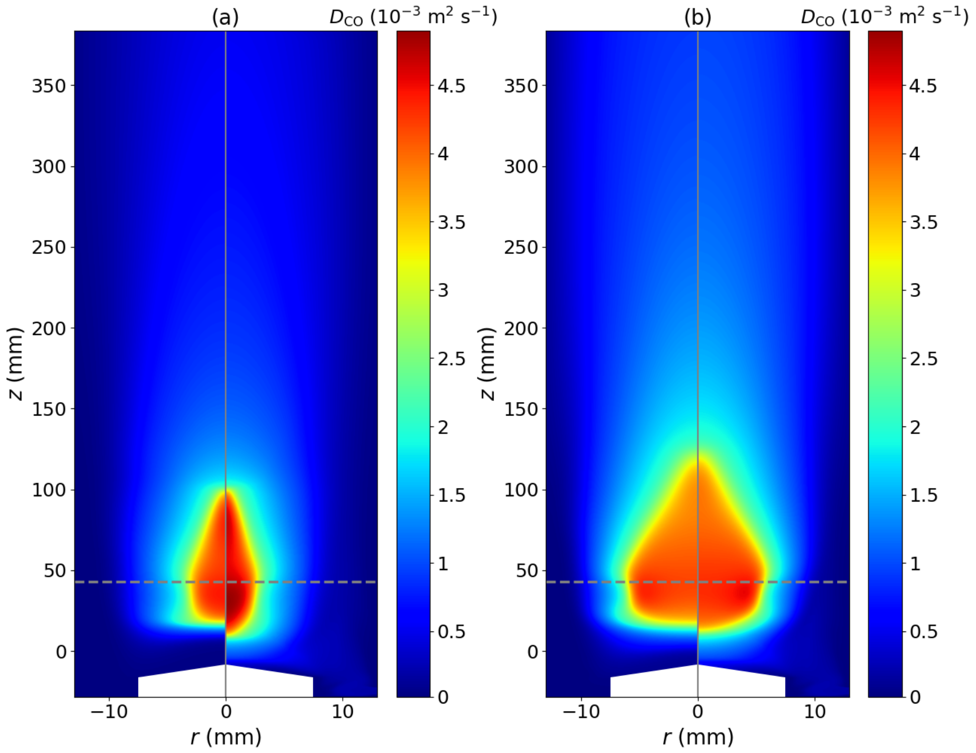

Figure S19: CO diffusivity calculated for $\phi = 20$ SLM and $P = 1100$ W (a) and 2900 W (b). In each panel, the results of the laminar flow and SST models are shown in the left-hand side and right-hand side, respectively. The dotted lines indicate the end of the microwave resonator.

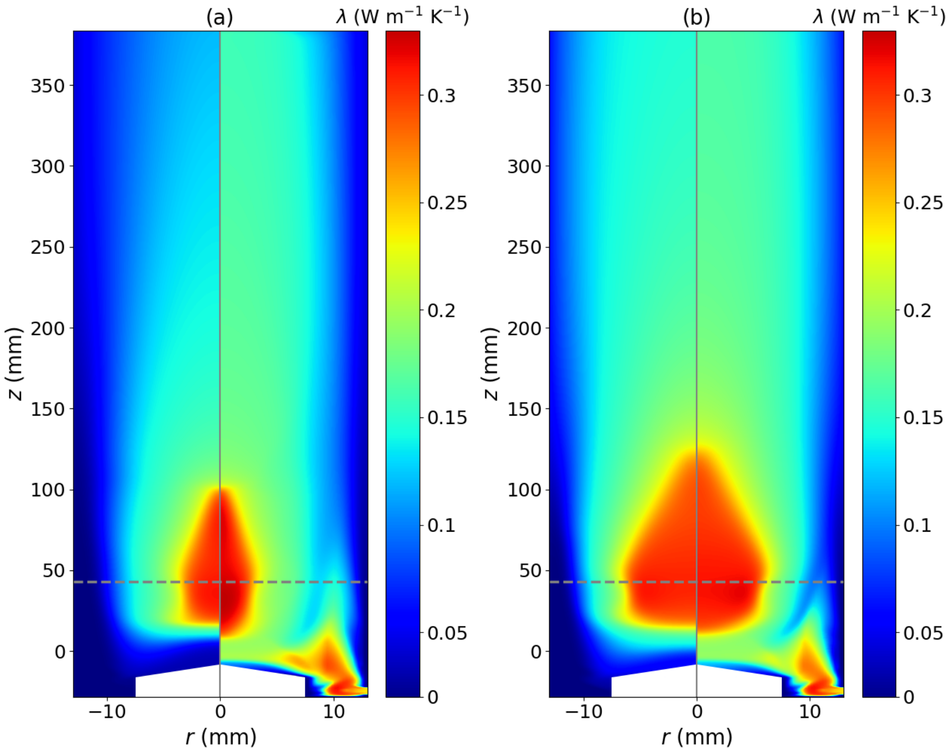

Figure S20: Thermal conductivity calculated for $\phi = 20$ SLM and $P = 1100$ W (a) and 2900 W (b). In each panel, the results of the laminar flow and SST models are shown in the left-hand side and right-hand side, respectively. The dotted lines indicate the end of the microwave resonator. Compare these two figures to Fig. 18–19, main text.

Finally, the figures below show our energy balance examples. First, in Fig. S21, the energy balance equation is solved in radial cut lines for $\phi = 20$ SLM.

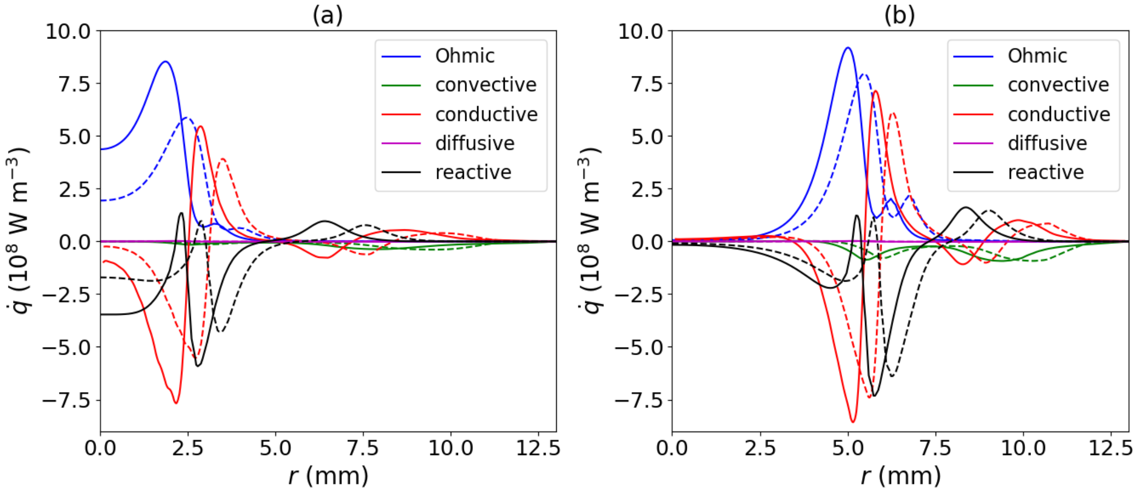

Figure S21: energy balance solved in radial cut lines for $\phi = 20$ SLM and $P = 1100$ W (a) and 2900 W (b). SST data are plotted as solid lines and laminar flow simulations are indicated by dashed lines. Compare this figure to Fig. 20, main text.

The heat rates copy the trends shown in Fig. 20, main text, and their magnitudes are overall smaller due to the lesser extent of plasma contraction (see, *e.g.*, Fig. 8, main text). These observations clearly support the conclusions in the main text, as does the energy balance plotted at $r = 0$ in Fig. S22.

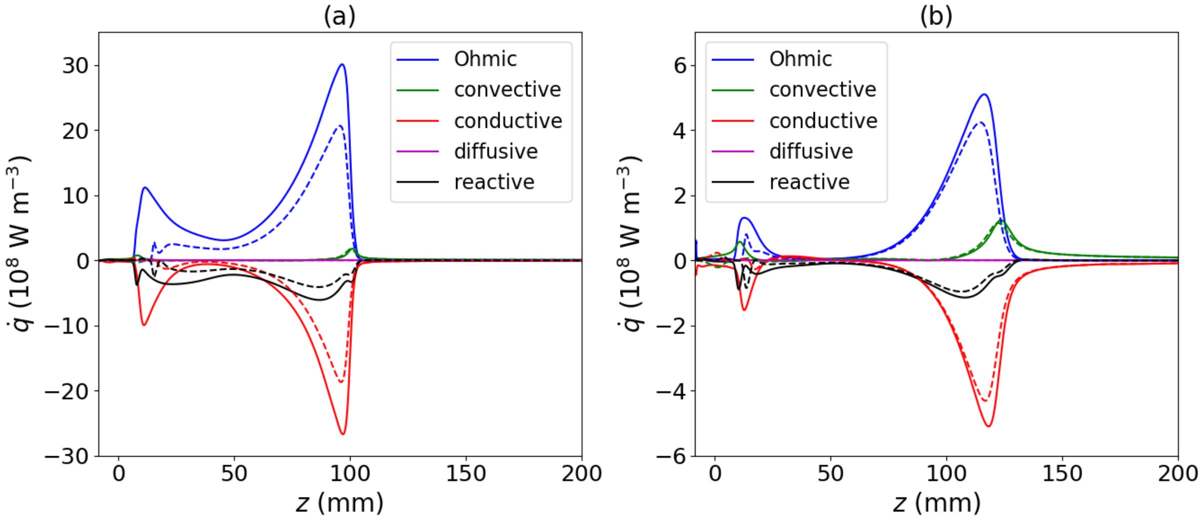

Figure S22: energy balance on the axis of symmetry for $\phi = 20$ SLM and $P = 1100$ W (a) and 2900 W (b). SST data are plotted as solid lines and laminar flow simulations are indicated by dashed lines. Compare this figure to Fig. 22, main text.

Here again, despite the lower flow rate, turbulence shows similar effects as in Fig. 22, main text. Namely, the turbulent flow develops two peaks in the Ohmic heat rate to balance the enhanced conductive cooling, and the heat rate values around the first peak are order-of-magnitude higher than in the laminar case. As in the main text, the differences are mitigated at elevated power. Finally, in Fig. S23–S24, we analyse the contributions to the reactive heat rate in both radial and axial cut lines.

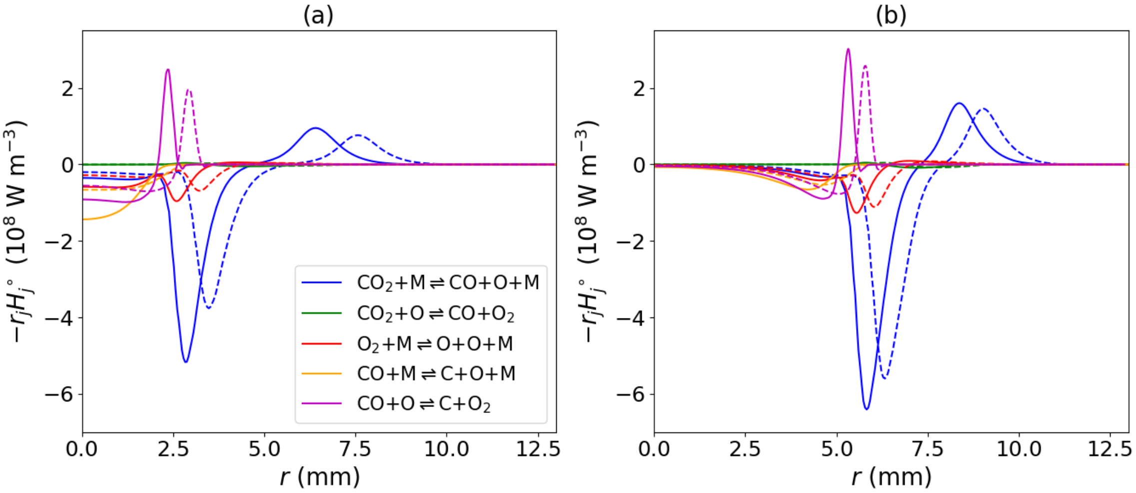

Figure S23: Heat sources of individual reactions contributing to the reactive heat rate in Fig. S21. SST data are plotted as solid lines and laminar flow simulations are indicated by dashed lines. Compare this figure to Fig. 21, main text.

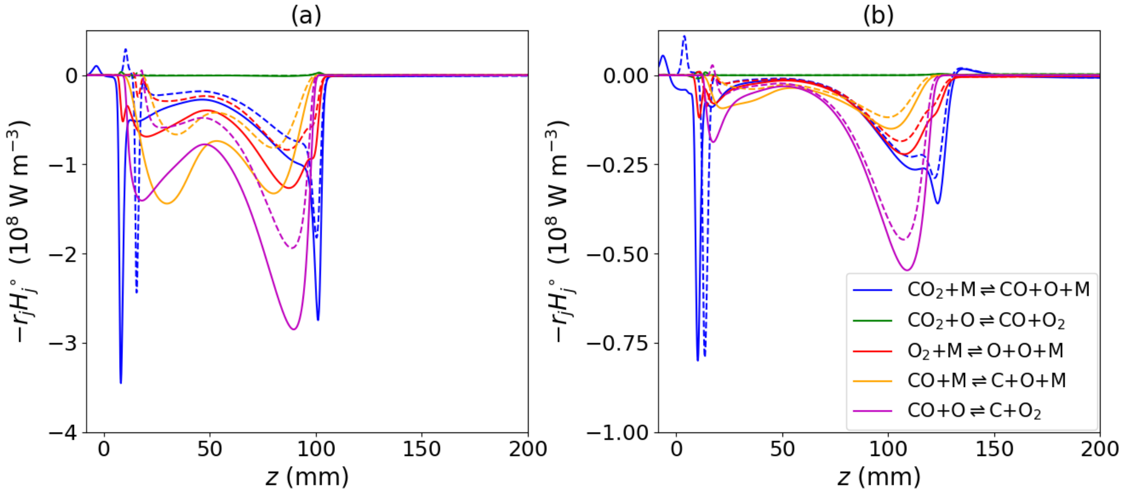

Figure S24: Heat sources of individual reactions contributing to the reactive heat rate in Fig. S22. SST data are plotted as solid lines and laminar flow simulations are indicated by dashed lines. In panel (a), the legend is dropped for graphical clarity; the colour code applies to both panels.

Fig. S23 mirrors the trends discussed in the main text (see Fig. 21, main text). In Fig. S24, most chemical reactions develop a heat sink, which corresponds to the endothermal splitting of molecular species inside the plasma. Interestingly, CO_2 splitting at the edges of the discharge shows the strongest heat sink, although, as indicated in Fig. 16, it is constrained to much smaller volumes than the discharge itself. In Fig. S25, this observation is confirmed for the 40 SLM case.

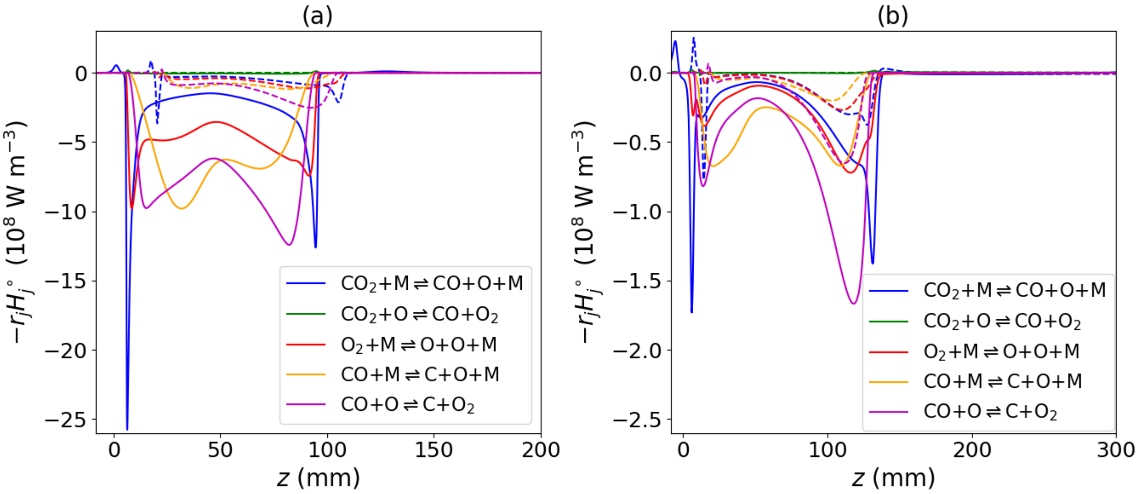

Figure S25: Heat sources of individual reactions contributing to the reactive heat rate in Fig. 22, main text. SST data are plotted as solid lines and laminar flow simulations are indicated by dashed lines. In panel (a), the legend is dropped for graphical clarity; the colour code applies to both panels.

In this figure, besides the order-of-magnitude difference in reactivity, the two flow models again show a visible discrepancy in axial positioning.

S7 Lewis Numbers

For a given species i, the Lewis number Le_i is defined as

$$\mathrm{Le}_i := \frac{\alpha_m}{D_i^m} = \frac{\frac{\lambda_m}{C_p\rho}}{D_i^m} \tag{S45}$$

and gauges the relevance of heat conduction relative to the mass diffusion of that species. α_m is the molecular heat diffusivity and the rest of the variables is defined in Sec. 2. The choice of molecular transport coefficients is justified because the corresponding ratio of turbulent diffusivities is consistently close to unity (in our case, $\alpha_\mathsf{T}/D_i^\mathsf{T} \in [0.98; 1.06]$ for all investigated data).

Fig. S26 plots the Lewis numbers for $i = \mathrm{CO}$, as solved by the SST model for both flow rates and powers investigated in the main text. Note that the colour bar scale is offset to begin at $\min\{\mathrm{Le}_{\mathrm{CO}}\} \doteq 0.7$.

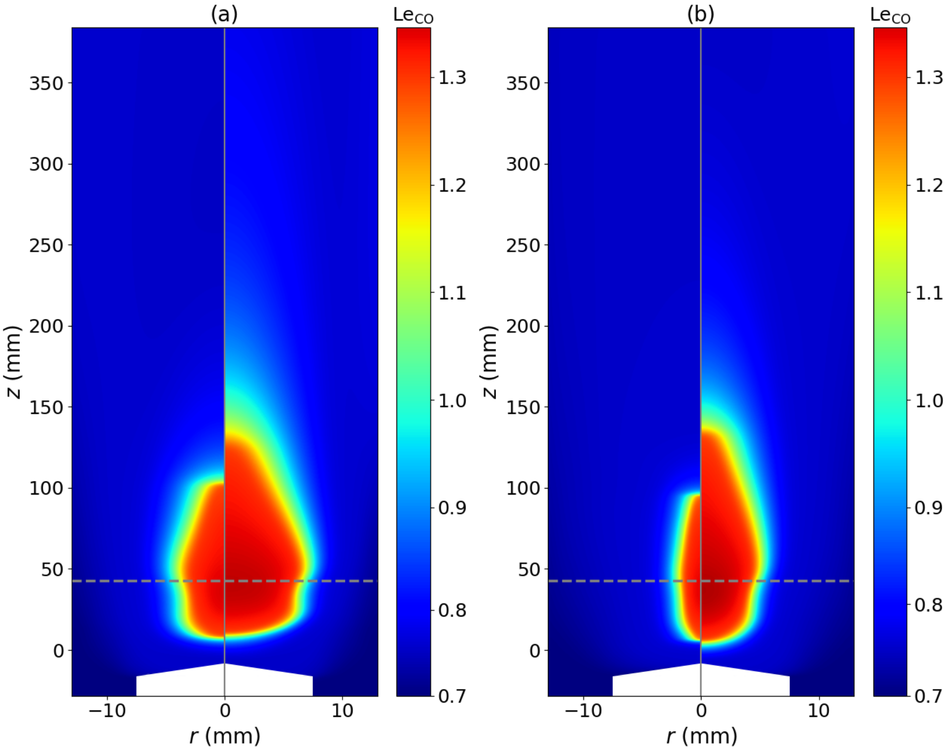

Figure S26: Lewis numbers of CO solved by the SST model for 20 SLM (a) and 40 SLM (b). The left- and right-hand sides of each panel correspond to 1100 W and 2900 W, respectively. The dotted lines indicate the end of the microwave resonator.

The figure shows that $\mathrm{Le}_{\mathrm{CO}}$ is a robust parameter; its distribution only varies in size but not in the range of values. Furthermore, the indicated range is insensitive to the choice of fluid flow model. We confirm this observation in Fig. S27 which shows the $\mathrm{Le}_{\mathrm{CO}}$ values solved by the laminar flow equations.

As in Fig. S26, the data show a spatial variation with the varying plasma shape, but the minimal and maximal values are the same for all tested conditions.

Le acts as an important scaling parameter in high-level turbulence models that describe the transport of chemically reactive species (see [63, 64] and the references therein). Notably, in the Le_i range indicated by Fig. S26–S27, it is found that turbulence is not the dominant mass transfer mechanism [63]. For this trend to change, Le_i should be limited to values below ~ 0.4 [63, 64], which is almost 2-times lower than the minimum of our data.

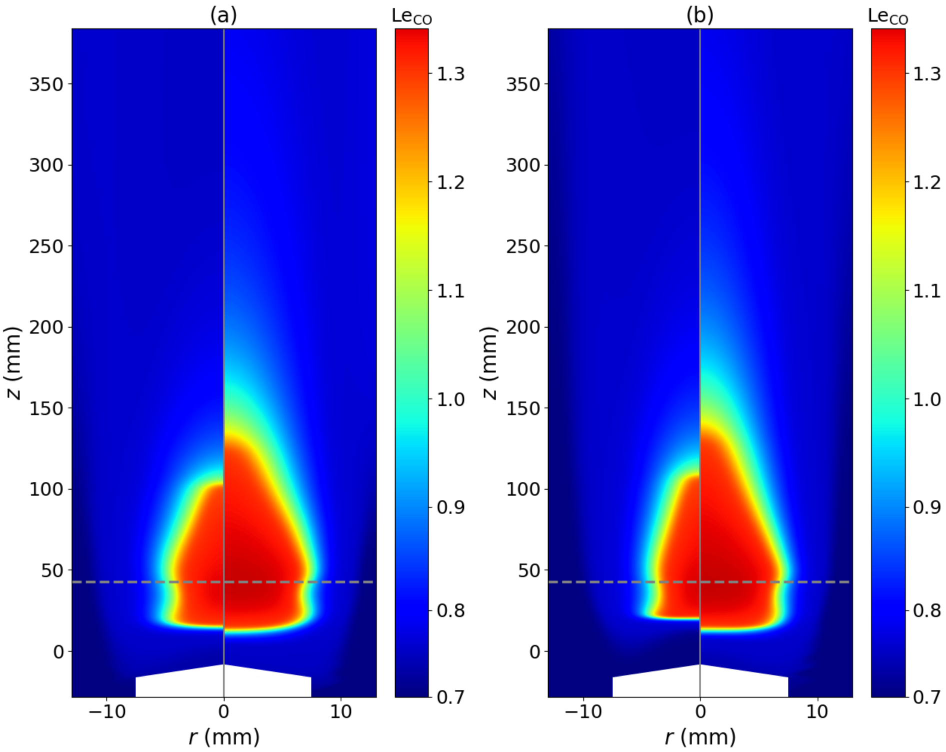

Figure S27: Lewis numbers of CO solved by the laminar flow model for 20 SLM (a) and 40 SLM (b). The left- and right-hand sides of each panel correspond to 1100 W and 2900 W, respectively. The dotted lines indicate the end of the microwave resonator.

In fact, such a decrease would require a considerable enhancement of the molecular diffusivity, which only happens at significantly lower molar masses. According to [64], this might be compatible with hydrogen species only.

Hence, our reactor performance results in Fig. 2 and 25 (main text) appear well justified. The main novelty of our work then lies in capturing the effects of turbulence on the plasma contraction dynamics, and hence on the distribution of reactive gas in the system. In another reactor geometry, turbulent heat transfer might be stronger, which might invoke a more significant difference in plasma size and CO_2 conversion. We recommend taking note of such effects in reactor design and in the future, we will revisit the conclusions of this study with a higher-level turbulence model.

References

(1) Menter, F. R.; Kuntz, M.; Langtry, R., et al. In *Turbulence, Heat and Mass Transfer*, 2003; Vol. 4, pp 625–632.

(2) Mercer, E. R.; Van Alphen, S.; van Deursen, C.; Righart, T.; Bongers, W.; Snyders, R.; Bogaerts, A.; van de Sanden, M.; Peeters, F. *Fuel* **2023**, *334*, 126734, DOI: `10.1016/j.fuel.2022.126734`.

(3) Van Alphen, S.; Hecimovic, A.; Kiefer, C. K.; Fantz, U.; Snyders, R.; Bogaerts, A. *Chemical Engineering Journal* **2023**, *462*, 142217, DOI: `10.1016/j.cej.2023.142217`.

(4) D'Isa, F. A.; Carbone, E. A.; Hecimovic, A.; Fantz, U. *Plasma Sources Science and Technology* **2020**, *29*, DOI: `10.1088/1361-6595/abaa84`.

(5) COMSOL AB, Stockholm, Sweden. COMSOL Multiphysics, v. 6.2, `www.comsol.com`, Accessed: 2024-05-25, 2024.

(6) Seibold, F.; Ligrani, P.; Weigand, B. *International Journal of Heat and Mass Transfer* **2022**, *187*, 122455, DOI: `10.1016/j.ijheatmasstransfer.2021.122455`.

(7) Pope, S. B., *Turbulent Flows*, 1st ed.; Cambridge University Press: 2000, DOI: `10.1017/CBO9780511840531`.

(8) McBride, B. J.; Zehe, M. J.; Gordon, S. NASA/TP–2002-211556: Glenn Coefficients for Calculating Thermodynamic Properties of Individual Species, `https://ntrs.nasa.gov/api/citations/20020085330/downloads/20020085330.pdf`, 2002.

(9) Bellemans, A.; Scoggins, J. B.; Jaffe, R.; Magin, T. E. *Physics of Fluids* **2019**, *31*, DOI: `10.1063/1.5119719`.

(10) Neufeld, P. D.; Janzen, A.; Aziz, R. A. *The Journal of Chemical Physics* **1972**, *57*, 1100–1102, DOI: `10.1063/1.1678363`.

(11) Moisan, M.; Pelletier, J.; Lister, G., *Physics of Collisional Plasmas: Introduction to high-frequency discharges*; Springer Netherlands: 2012; Vol. 9789400745582, DOI: `10.1007/978-94-007-4558-2`.

(12) Baeva, M.; Stankov, M.; Trautvetter, T.; Methling, R.; Hempel, F.; Loffhagen, D.; Foest, R. *Journal of Physics D: Applied Physics* **2021**, *54*, 355205, DOI: `10.1088/1361-6463/ac08cc`.

(13) Vialetto, L.; van de Steeg, A.; Viegas, P.; Longo, S.; Van Rooij, G.; van de Sanden, M.; van Dijk, J.; Diomede, P. *Plasma Sources Science and Technology* **2022**, *31*, 055005, DOI: `10.1088/1361-6595/ac56c5`.

(14) Viegas, P.; Vialetto, L.; Wolf, A.; Peeters, F.; Groen, P.; Righart, T.; Bongers, W.; Van de Sanden, M.; Diomede, P. *Plasma Sources Science and Technology* **2020**, *29*, 105014, DOI: `10.1088/1361-6595/abb41c`.

(15) Herzberg, G., *Molecular Spectra and Molecular Structure Infrared II. Infrared and raman Spectra of Polyatomic Molecules.* 7nd; Van Nostrand Company Inc.: 1945.

(16) Hagelaar, G. J.; Pitchford, L. C. *Plasma Sources Science and Technology* **2005**, *14*, 722–733, DOI: `10.1088/0963-0252/14/4/011`.

(17) Jimenez-Diaz, M.; Carbone, E. A.; Dijk, J. V.; Mullen, J. J. V. D. *Journal of Physics D: Applied Physics* **2012**, *45*, DOI: `10.1088/0022-3727/45/33/335204`.

(18) Georgieva, V.; Berthelot, A.; Silva, T.; Kolev, S.; Graef, W.; Britun, N.; Chen, G.; van der Mullen, J.; Godfroid, T.; Mihailova, D., et al. *Plasma processes and polymers* **2017**, *14*, 1600185, DOI: `10.1002/ppap.201600185`.

(19) Kabouzi, Y.; Graves, D.; Castaños-Martínez, E.; Moisan, M. *Physical Review E – Statistical, Nonlinear, and Soft Matter Physics* **2007**, *75*, 016402, DOI: 10.1103/PhysRevE.75.016402.

(20) Baeva, M.; Bösel, A.; Ehlbeck, J.; Loffhagen, D. *Physical Review E—Statistical, Nonlinear, and Soft Matter Physics* **2012**, *85*, 056404, DOI: 10.1103/PhysRevE.85.056404.

(21) Lowke, J.; Phelps, A.; Irwin, B. *Journal of Applied Physics* **1973**, *44*, 4664–4671, DOI: https://doi.org/10.1063/1.1662017.

(22) Biondo, O.; Fromentin, C.; Silva, T.; Guerra, V.; van Rooij, G.; Bogaerts, A. *Plasma Sources Science and Technology* **2022**, *31*, 074003, DOI: 10.1088/1361-6595/ac8019.

(23) Pietanza, L.; Colonna, G.; Capitelli, M. *Physics of Plasmas* **2020**, *27*, DOI: 10.1063/1.5139625.

(24) Park, C.; Howe, J. T.; Jaffe, R. L.; Candler, G. V. *Journal of Thermophysics and Heat transfer* **1994**, *8*, 9–23, DOI: 10.2514/3.496.

(25) Albrechts, M.; Tsonev, I.; Bogaerts, A. *Plasma Sources Science and Technology* **2024**, *33*, 045017, DOI: 10.1088/1361-6595/ad3f4a.

(26) Annušová, A.; Marinov, D.; Booth, J.-P.; Sirse, N.; Da Silva, M. L.; Lopez, B.; Guerra, V. *Plasma Sources Science and Technology* **2018**, *27*, 045006, DOI: 10.1088/1361-6595/aab47d.

(27) Beuthe, T. G. B. T. G.; Chang, J.-S. C. J.-S. *Japanese Journal of Applied Physics* **1997**, *36*, 4997, DOI: 10.1143/JJAP.36.4997.

(28) Koelman, P.; Heijkers, S.; Tadayon Mousavi, S.; Graef, W.; Mihailova, D.; Kozak, T.; Bogaerts, A.; van Dijk, J. *Plasma Processes and Polymers* **2017**, *14*, 1600155, DOI: 10.1002/ppap.201600155.

(29) Tsonev, I.; Biondo, O.; Bogaerts, A. *Plasma Sources Science and Technology* **2025**.

(30) Biagi database. LXCat, www.lxcat.net, Accessed: 2024-02-11, 2024.

(31) Itikawa database. LXCat, www.lxcat.net, Accessed: 2024-02-11, 2024.

(32) IST-Lisbon database. LXCat, www.lxcat.net, Accessed: 2024-02-11, 2024.

(33) IAA database. LXCat, www.lxcat.net, Accessed: 2024-02-11, 2024.

(34) BSR database. LXCat, www.lxcat.net, Accessed: 2024-02-11, 2024.

(35) Polak, L.; Slovetsky, D. *International Journal for Radiation Physics and Chemistry* **1976**, *8*, 257–282, DOI: 10.1016/0020-7055(76)90070-X.

(36) Cosby, P. *The Journal of Chemical Physics* **1993**, *98*, 7804–7818, DOI: 10.1063/1.464588.

(37) Cosby, P. *The Journal of Chemical Physics* **1993**, *98*, 9560–9569, DOI: 10.1063/1.464387.

(38) Itikawa, Y. *Journal of Physical and Chemical Reference Data* **2002**, *31*, 749–767, DOI: 10.1063/1.1481879.

(39) Albritton, D. *Atomic Data and Nuclear Data Tables* **1978**, *22*, 1–89, DOI: 10.1016/0092-640X(78)90027-X.

(40) McElroy, D.; Walsh, C.; Markwick, A.; Cordiner, M.; Smith, K.; Millar, T. *Astronomy & Astrophysics* **2013**, *550*, A36, DOI: 10.1051/0004-6361/201220465.

(41) Kossyi, I.; Kostinsky, A. Y.; Matveyev, A.; Silakov, V. *Plasma Sources Science and Technology* **1992**, *1*, 207, DOI: 10.1088/0963-0252/1/3/011.

(42) University of California, Berkeley. GRI–Mech 3.0 Database, `http://combustion.berkeley.edu/gri-mech/`, Accessed: 2024-05-25, 2024.

(43) Mick, H.-J.; Burmeister, M.; Roth, P. *AIAA Journal* **1993**, *31*, 671–676, DOI: `10.2514/3.11602`.

(44) Kruse, T.; Roth, P. *The Journal of Physical Chemistry A* **1997**, *101*, 2138–2146, DOI: `10.1021/jp963373o`.

(45) Phelps database. LXCat, `www.lxcat.net`, Accessed: 2024-02-11, 2024.

(46) Ridenti, M. A.; Amorim, J. D.; Pino, A. D.; Guerra, V.; Petrov, G. *Physical Review E* **2018**, *97*, DOI: `10.1103/PhysRevE.97.013201`.

(47) Zhang, W.; Tao, J.; Huang, K.; Wu, L. *IEEE Transactions on Plasma Science* **2017**, *45*, 2929–2939, DOI: `10.1109/TPS.2017.2759501`.

(48) Kim, G.; Kang, W.; Bak, M. S. *Journal of Physics D: Applied Physics* **2025**, *58*, DOI: `10.1088/1361-6463/ade9d6`.

(49) Zhang, W.; Wu, L.; Huang, K.; Tao, J. *Physics of Plasmas* **2019**, *26*, DOI: `10.1063/1.5086088`.

(50) Moisan, M.; Zakrzewski, Z. *Journal of Physics D: Applied Physics* **1991**, *24*, DOI: `10.1088/0022-3727/24/7/001`.

(51) Leins, M. Development and Spectroscopic Investigation of a Microwave Plasma Source for the Decomposition of Waste Gases, Ph.D. Thesis, Universität Stuttgart, 2010, `https://elib.uni-stuttgart.de/bitstream/11682/1890/1/Dissertation_Leins.pdf`.

(52) COMSOL AB, Stockholm, Sweden. In-plane mirowave plasma (application ID 8664). COMSOL Multiphysics, v. 6.2, `https://www.comsol.com/model/in-plane-microwave-plasma-8664`, Accessed: 2024-05-25, 2024.

(53) Leins, M.; Alberts, L.; Kaiser, M.; Walker, M.; Schulz, A.; Schumacher, U.; Stroth, U. *Plasma Processes and Polymers* **2009**, *6*, S227–S232, DOI: `10.1002/ppap.200930604`.

(54) Balanis, C. A., *Advanced Engineering Electromagnetics*, 2nd ed.; Wiley: 2012, DOI: `10.1002/9781394180042`.

(55) Viegas, P.; Vialetto, L.; van de Steeg, A. W.; Wolf, A.; Bongers, W. A.; van Rooij, G. J.; van de Sanden, M.; Diomede, P.; Peeters, F. *Plasma Sources Science and Technology* **2021**, *30*, 065022, DOI: `10.1088/1361-6595/ac04bd`.

(56) Groen, P. W. C.; Wolf, A.; Righart, T.; Van De Sanden, M.; Peeters, F.; Bongers, W. *Plasma Sources Science and Technology* **2019**, *28*, 075016, DOI: `10.1088/1361-6595/ab1ca1`.

(57) Wolf, A.; Righart, T.; Peeters, F.; Groen, P.; Van De Sanden, M.; Bongers, W. *Plasma Sources Science and Technology* **2019**, *28*, 115022, DOI: `10.1088/1361-6595/ab4e61`.

(58) Hickstein, D. D.; Gibson, S. T.; Yurchak, R.; Das, D. D.; Ryazanov, M. *Review of Scientific Instruments* **2019**, *90*, DOI: `10.1063/1.5092635`.

(59) PyAbel PyAbel: v0.9.0, `https://zenodo.org/records/7438595`, Accessed: 2025-03-10, 2025.

(60) Van Poyer, H. M.; Tsonev, I.; Maerivoet, S. J.; Albrechts, M. C.; Bogaerts, A. *Chemical Engineering Journal* **2025**, *507*, 160688, DOI: `10.1016/j.cej.2025.160688`.

(61) Hecimovic, A.; Kiefer, C.; Meindl, A.; Antunes, R.; Fantz, U. *Journal of CO_2 Utilization* **2023**, *71*, DOI: `10.1016/j.jcou.2023.102473`.

(62) Shigeta, M. *Journal of Physics D: Applied Physics* **2016**, *49*, DOI: 10.1088/0022-3727/49/49/493001.

(63) Chakraborty, N.; Swaminathan, N. *Combustion Science and Technology* **2010**, *182*, 1201–1240, DOI: 10.1080/00102201003639276.

(64) Aspden, A. J.; Day, M. S.; Bell, J. B. *Proceedings of the Combustion Institute* **2011**, *33*, 1473–1480, DOI: 10.1016/j.proci.2010.05.095.